Structure of the human CTF18–RFC clamp loader bound to PCNA

Giuseppina R. Briola[1¶], Muhammad Tehseen[1¶], Amani Al-Amodi[1], Grace Young[2], Ammar U. Danazumi[1], Phong Quoc Nguyen[1], Christos G. Savva[1], Mark Hedglin[2], Samir M. Hamdan[1,3*] and Alfredo De Biasio[1*]

[1]Bioscience Program, Division of Biological and Environmental Sciences and Engineering, King Abdullah University of Science and Technology, Thuwal 23955, Saudi Arabia.

[2]Department of Chemistry, The Pennsylvania State University, University Park, PA, USA 16802

[3]KAUST Center of Excellence for Smart Health, King Abdullah University of Science and Technology, Thuwal 23955, Saudi Arabia.

*Corresponding authors

E-mail: samir.hamdan@kaust.edu.sa or alfredo.debiasio@kaust.edu.sa

¶These authors contributed equally to this work.

Abstract

Sliding clamps like PCNA are crucial processivity factors for replicative polymerases, requiring specific clamp loaders for loading onto DNA. The human alternative clamp loader CTF18-RFC interacts with the leading strand polymerase Pol ε and loads PCNA onto primer/template DNA using its RFC pentameric module. Here, we provide a structural characterization of the human CTF18-RFC complex and its interaction with PCNA. Our cryo-EM data support that the Ctf8 and Dcc1 subunits of CTF18-RFC, which form the regulatory module interacting with Pol ε, are flexibly tethered to the RFC module. A 2.9 Å cryo-EM structure shows the RFC module bound to PCNA in an auto-inhibited conformation similar to the canonical RFC loader, marking the initial step of the clamp-loading reaction. The unique RFC1 (Ctf18) large subunit of CTF18-RFC, which based on the cryo-EM map shows high relative flexibility, is anchored to PCNA through an atypical low-affinity PIP box in the AAA+ domain and engages the RFC5 subunit using a novel β-hairpin at the disordered N-terminus. We show that deletion of this β-hairpin impairs the CTF18-RFC–PCNA complex stability, slows down clamp loading, and decreases the rate of primer synthesis by Pol ε. Our research identifies distinctive structural characteristics of the human CTF18-RFC complex, providing insights into its role in PCNA loading and the stimulation of leading strand synthesis by Pol ε.

Introduction

High fidelity and efficiency are critical for chromosomal DNA duplication in eukaryotes. This precision is achieved through the coordinated action of replicative DNA polymerases,

45 Pol δ and Pol ε, anchored to the sliding clamp, Proliferating Cell Nuclear Antigen (PCNA)
46 (1). The ring-shaped PCNA homotrimer encircles DNA, enhancing the processivity of
47 these polymerases in DNA replication and repair processes, including excision repair and
48 homologous recombination (2), and plays an important role in sister chromatid cohesion
49 establishment (3). The closed-ring topology of PCNA necessitates the transient opening
50 of one interface to facilitate the incorporation and trapping of primer-template DNA. This
51 critical function is executed by pentameric AAA+ (Adenosine Triphosphatase Associated)
52 ATPases, collectively known as clamp loaders (4-6). Extensive structural and biochemical
53 work in different organisms (7-12) established a common mechanism for the clamp-
54 loading reaction, which proceeds through three main steps (13-18). Initially, the clamp
55 loader engages with the intact clamp ring, adopting an autoinhibited configuration that
56 precludes DNA binding (10). This stage sets the groundwork for the subsequent
57 transition, where the clamp loader alters its conformation to an activated state. This
58 change facilitates the opening of the clamp ring, creating a gap sufficiently large to permit
59 the passage of duplex DNA and aligning the clamp loader for primer-template DNA
60 interaction. The final phase of this process is initiated by the binding of DNA to the clamp
61 loader, catalysing ATP hydrolysis. DNA binding prompts the closure of the clamp and
62 hydrolysis of ATP induces the concurrent disassembly of the closed clamp loader from
63 the sliding clamp-DNA complex, completing the cycle necessary for the engagement of
64 the replicative polymerases to start DNA synthesis.

65 The canonical Replication Factor C (RFC), consisting of a large RFC1 subunit and
66 four subunits (RFC2, RFC3, RFC4, and RFC5), acts as the primary clamp loader for
67 PCNA (4, 19). However, eukaryotes also employ alternative loaders (20), including

68 CTF18-RFC (6, 21-24), which likely use a conserved loading mechanism but are
69 functionally specialized through specific protein interactions and context-dependent roles
70 in DNA replication.

71 Genome-wide analyses revealed that CTF18-RFC predominantly facilitates PCNA
72 loading on the leading strand, in contrast to the canonical RFC complex, which mainly
73 loads PCNA on the lagging strand (25). Although CTF18-RFC is not essential for bulk
74 DNA replication in yeast (26, 27), it plays a vital role in ensuring sister chromatid cohesion
75 (21, 28, 29). This may be due to its selective loading of PCNA linked to EcoI
76 acetyltransferase (3), which acetylates Smc3, preventing cohesin destabilization by WapI
77 (30-32). Recruitment of CTF18-RFC to the leading strand is also important for activation
78 of the replication checkpoint (22, 24, 33, 34).

79 The CTF18-RFC complex features two distinct modules with separate functions
80 (23, 28, 35, 36): a catalytic RFC module for PCNA loading, consisting of a large RFC1-
81 like subunit (hereby referred to as Ctf18), alongside the four RFC2, RFC3, RFC4 and
82 RFC5 subunits utilized by the canonical RFC complex, and a regulatory module, made
83 up of the Ctf8 and Dcc1 subunits. These latter two subunits attach to the Ctf18 C-
84 terminus, forming the Ctf18-1-8 module. A long linker predicted to be flexible connects
85 these two segments (34, 37). Structural and functional studies have demonstrated that
86 the interaction between the Ctf18-1-8 module and the catalytic domain of Pol2 ($Pol2_{CAT}$),
87 the principal subunit of Pol ε, directs CTF18-RFC to replication forks and boosts its clamp
88 loading efficiency (34, 37). This interaction situates the clamp loader close to the
89 primer/template junction, facilitating PCNA loading (34). $Pol2_{CAT}$ is tethered to the
90 remainder of Pol ε via an unstructured linker, making it an integral component of the

91 CMGE (Cdc45-Mcm-GINS-Pol ε) core replisome complex (38). It has been proposed that
92 Pol ε utilizes both the CMG helicase and PCNA as processivity factors to facilitate normal
93 replication rates (39, 40). Tethering by the CMG complex might allow Pol ε to dissociate
94 from the 3′ end of the leading strand but stay at the replication fork until leading strand
95 synthesis restarts. Given the relatively weak interaction of Pol ε with PCNA (41), it is
96 possible that multiple PCNA loading events on the leading strand via CTF18-RFC are
97 necessary to achieve full Pol ε processivity.

98 Although the structure of the Ctf18-1-8 module in association with $Pol2_{CAT}$ has
99 been elucidated (34, 37), the architecture of the CTF18-RFC module and its interaction
100 with PCNA remain uncharacterized. To investigate the clamp loading mechanism
101 employed by CTF18-RFC, we reconstituted the full human CTF18-RFC complex with
102 PCNA and determined its structure using cryo-electron microscopy (cryo-EM). Our cryo-
103 EM data supports the prediction that the Ctf18-1-8 and RFC modules are flexibly tethered.
104 The analysis yielded high-resolution reconstructions of the entire CTF18-RFC module
105 bound to a closed PCNA ring. Although the overall architecture mirrors the autoinhibited
106 state observed in the canonical RFC loader in a complex with PCNA (10), distinctive
107 features within CTF18-RFC were identified. These distinctions may offer insights into the
108 specialized functional roles CTF18-RFC plays in DNA replication.

109

110 Results

111 Structure of the human CTF18-RFC–PCNA complex

112 We employed single-particle cryo-EM to determine the structure of human CTF18-
113 RFCbound to PCNA. To this purpose, the full CTF18-RFC complex, including Ctf8 and
114 Dcc1, was expressed in insect cells and purified to homogeneity (Fig S1). The purified
115 complex includes all subunits as shown in the SDS-PAGE gel (Fig S1). With the aim of
116 trapping CTF18-RFCin different steps of the clamp loading reaction, the complex was
117 vitrified in the presence of ATP, PCNA, and primer/template DNA but omitting the Mg^{2+}
118 cofactor to halt hydrolysis (42), and then imaged by cryo-EM (Fig S2). Surprisingly, image
119 processing yielded only a major 3D class, including the CTF18-RFC pentamer bound to
120 a closed PCNA ring (Fig 1a-b, Fig S2-3), with no evidence of DNA density. The Ctf18-1-8
121 module, which is connected to the RFC module by a 91 amino acid linker (Fig 1a), is not
122 resolved in the map (Fig 1b), suggesting it is flexibly tethered to the RFC module. The
123 map was refined to a global resolution of 2.9 Å (Fig S2-3), which allowed model building
124 of the five CTF18-RFC subunits as well as the PCNA homotrimer (Fig 1c). The final model
125 refines to a map-to-model FSC of 3.0 Å at 0.5 threshold, with good refinement statistics
126 (S1 Table).

127 The five CTF18-RFC subunits are positioned on top of the closed PCNA ring,
128 which is planar and undistorted (Fig 1c). A structural comparison shows that the CTF18-
129 RFC pentamer was trapped in an autoinhibited conformation analogous to that reported
130 for the canonical human (h) and yeast (sc) RFC (8, 10), pertaining to the initial step of the
131 clamp loading reaction, right before clamp opening (Fig 1d). In such conformation, the
132 AAA+ domains form an overtwisted and asymmetric spiral that is incompatible with DNA
133 binding (8, 10). The AAA+, collar, and A' domains of the Ctf18 subunit (Fig 2a) align with
134 the homologous domains of hRFC1 (Fig 2b). As in the hRFC structure (10), the Ctf18

135 subunit interacts with RFC2, RFC3, and PCNA-I. Three main deviations from the
136 hRFC–PCNA structure are observed (10): a different tilt of the PCNA ring (Fig 1c-d),
137 significant mobility of the large Ctf18 subunit (Fig 1b and Fig S2) and, importantly, the
138 presence of a β-hairpin engaged to the outer surface of the RFC5 subunit, which we
139 mapped to the disordered N-terminus of the Ctf18 subunit (Fig 2a and 2c). These features
140 are analyzed in detail below.

141 Structure of the large subunit of CTF18-RFC

142 The Ctf18 subunit presents 26% identity with the homologous subunit RFC1 of hRFC and
143 an overall structural conservation, with some deviations particularly in the A' domain (Fig
144 2b). Compared to the other subunits, the AAA+ domain of Ctf18 shows increased
145 flexibility, as evidenced by the local resolution map of the complex as well as 3D variability
146 analysis (43, 44) (Fig S2d and Supplementary Video 1). Increased flexibility was not
147 detected in the RFC1 subunit of human RFC bound to PCNA (10). This discrepancy could
148 be explained by diminished inter-subunit interactions involving both the AAA+ and collar
149 domains of Ctf18 compared to RFC1, as illustrated in Fig S4: the AAA+ domain of Ctf18
150 forms fewer stabilizing salt bridges and h-bonds with RFC2 than RFC1 does, and the
151 Ctf18 collar domain establishes markedly weaker interactions with both RFC2 and RFC3
152 than the extensive network observed for RFC1. Conversely, the interaction between the
153 A' domain of CTF18-RFC and RFC3 is strong as observed for RFC. Overall, the total
154 buried surface area between Ctf18 and interacting subunits is comparable to that of RFC1
155 (~5500 Å² versus ~5300 Å²). However, the buried surface area between Ctf18 and RFC2
156 is markedly smaller than that of RFC1 (~1400 Å² and ~2300 Å²). As explained below, the
157 lost interactions mediated by the AAA+ and collar domains of Ctf18 are partially

158 counterbalanced by those established with the N-terminal β-hairpin, which is absent in
159 the canonical RFC. Additionally, the interaction between Ctf18 and PCNA is weaker
160 compared to the interaction between RFC1 and PCNA, further contributing to these
161 structural differences (see next section). The Ctf18 C-terminal region (residues 953-975)
162 predicted to interact with the Ctf8 and Dcc1 subunits (Fig 2a) is invisible in the map.

163 The most striking feature is a small β-hairpin-containing fold mapped between
164 residues 165-194 in the disordered N-terminus (Fig 2a and 2c) of the Ctf18 subunit, ~80
165 Å apart from the Ctf18 AAA+ domain, to which it is connected by a disordered linker of 86
166 amino acids (residues 195-280). This N-terminal fold plugs into a groove at the outer
167 surface of the collar domain of the RFC5 subunit defined by helices α1, α3, α4, and α5
168 (Fig 3a). The resolution of the map in this region is sufficient for confident model building
169 of the interface (Fig 3b). The interface buries 984 $Å^2$ and is characterized by both apolar
170 and polar interactions (Fig 3a). A set of hydrophobic side chains protruding from Ctf18 β-
171 hairpin (V178, V180, L190, L192) approaches a complementary patch of hydrophobic
172 residues on RFC5 (L255 in α1; F287, V291 and F293 in α3; I336 and V337 in α5). The
173 interface is further strengthened by several hydrogen bonds mostly mediated by main-
174 chain atoms in the Ctf18 β-hairpin, and by a salt bridge between R193 of the Ctf18 β-
175 hairpin and D292 of RFC5. It is worth highlighting that RFC2 separates the Ctf18 and
176 RFC5 subunits. Despite this separation, Ctf18 projects the β-hairpin directly onto RFC5,
177 bypassing any interactions with RFC2 (Fig 2c). This observation supports that the β-
178 hairpin functions as a “latch” to stabilize the CTF18-RFC structure.

179 Similarly to human CTF18-RFC, long regions predicted to be disordered by
180 AlphaFold (45) are present in the N-terminal sequence of Ctf18 of lower eukaryotes. The

181 β-hairpin region of human Ctf18 does not show strict sequence conservation, but a similar
182 fold in the N-terminus of lower eukaryotes Ctf18 is predicted (Fig 2a). Therefore, lower
183 eukaryotes may use a similar β-hairpin motif to bind the corresponding subunit of the
184 RFC-module complex (RFC5 in human, Rfc3 in *S. cerevisiae)*, emphasizing its
185 importance.

186 Interactions of CTF18-RFC with PCNA

187 CTF18-RFC engages two of the three PCNA protomers through four contact points
188 involving the AAA+ domains of Ctf18, RFC2, RFC4, and RFC5 (Fig 1c and Fig 3c). The
189 interactions of PCNA with the RFC2 and RFC5 subunits are analogous to those reported
190 in the hRFC–PCNA complex (10). However, while Ctf18 engages PCNA-I via a PIP-box
191 interaction similar to hRFC1 (10), its atypical PIP motif — lacking aromatic residues (Fig.
192 2a and Fig. 3c) — results in a smaller buried surface area (~780 Å² vs. ~1010 Å²). A
193 methionine residue (M419) inserts into the so-called "Q-pocket," which is typically
194 occupied by a glutamine in canonical PIP-boxes, while V422 occupies the conserved
195 hydrophobic pocket that usually accommodates aromatic residues. This low-affinity
196 interaction does not stably anchor Ctf18 to PCNA-I and may contribute to the relative
197 flexibility of the AAA+ domain of Ctf18 observed in the complex (Fig S2 and
198 Supplementary Video 1). The PIP-box of RFC5 is also atypical but contains two
199 hydrophobic residues (I114 and F115) that insert into the conserved pocket of PCNA-II.
200 The interacting motifs of RFC2 and RFC4 differ from each other in sequence but both
201 engage similar regions involving the interdomain connecting loop (IDCL) of PCNA-I and
202 PCNA-II, respectively (Fig 3d).

203 Interestingly, while RFC4 interacts with PCNA in the CTF18-RFC complex, it does
204 not in the hRFC–PCNA complex (10). The RFC4–PCNA interaction, which was also
205 observed in the structure of *S. cerevisiae* RFC bound to open PCNA (11), brings PCNA
206 closer to the CTF18-RFC module, thereby explaining the distinct tilt of the PCNA ring
207 observed in our structure compared to the hRFC–PCNA complex (Fig. 1c and 1d). Given
208 the structure of scRFC bound to open PCNA (11), where all five RFC subunits are bound
209 to PCNA (Fig 3d), we predict that a conformational shift in CTF18–RFC, specifically
210 bringing the fifth subunit (RFC3) to engage PCNA-III, would be necessary to disrupt the
211 interface between PCNA-I and PCNA-III, thereby opening the clamp and aligning the
212 CTF18-RFC subunits for primer-template DNA interaction. The reason for the absence of
213 such an active CTF18-RFC conformation in our cryo-EM analysis remains uncertain.
214 However, similar to observations with the hRFC–PCNA complex, where an open-clamp
215 state was not reported (10), this could be attributed to the hydrophobic regions of the
216 open clamp interacting with the water-air interface, potentially leading to protein
217 denaturation during the vitrification process to prepare the cryo-EM grids.
218

219 Nucleotide binding to the AAA+ modules

220 The map is consistent with nucleotides in four of the five AAA+ domains of the CTF18-
221 RFC subunits (Fig 4a). ATP is bound to subunits Ctf18, RFC2, and RFC5, while ADP
222 appears to engage RFC3, consistent with the structure of the hRFC–PCNA complex
223 reconstituted with the slowly hydrolysable nucleotide ATPγS (10). Density for the adenine
224 ring of ATP in the Ctf18 subunit is poor, likely a consequence of the increased mobility of
225 the AAA+ domain of this subunit (Fig 4a). Compared to the canonical RFC1, the Walker

226 A motif of Ctf18 contains a leucine residue (L378) instead of a valine, but this substitution
227 does not appear to affect its interaction with the ATP nucleotide (Fig S5). Since RFC3
228 lacks critical catalytic residues and bears a substitution in the Walker A motif (10), the
229 presence of ADP, rather than a product of ATP hydrolysis, probably results from co-
230 purification of the complex where ADP contaminants are present. In the human RFC
231 complex, it has been previously shown that an intact nucleotide binding site in RFC3 has
232 an important structural role in the complex assembly (46, 47). If this is the case for CTF18-
233 RFC, it remains to be established, but it is likely that ADP binding to this subunit may play
234 a stabilizing role in all RFC-like loaders.

235 Differently from the hRFC–PCNA complex, where RFC4 is bound to ATPγS, in
236 CTF18-RFC, this subunit is not engaged with a nucleotide (Fig 4a). The residues in the
237 AAA+ of RFC4 of CTF18-RFC coordinated to ATPγS in hRFC are displaced and
238 incompatible with nucleotide binding (Fig 4c). In particular, the side chains of R45 and
239 P46 in RFC4 occupy the space where ATP would normally bind, thereby sterically
240 hindering nucleotide accommodation in the CTF18-RFC structure (Fig 4c). Interestingly,
241 mutation of the conserved K84 residue in the ATP-binding motif of RFC4 in hRFC did not
242 impair the ability of this subunit to assemble with other RFC subunits (46, 47). In
243 agreement, our structure shows that the lack of ATP binding to RFC4 does not preclude
244 the assembly of the CTF18-RFC pentamer in the autoinhibited conformation. However,
245 considering the importance of ATP binding of RFC4 for the hRFC clamp loading function
246 (48-51), it is expected that ATP binding to RFC4 in CTF18-RFC is required to switch to
247 an enzymatically active conformation.

248 The asymmetric spiral of the CTF18-RFC AAA+ pentamer (Fig 4a-b) disrupts the
249 active sites at the Ctf18/RFC2, RFC2/5, and RFC5/4 interfaces (Fig 4c). At these
250 interfaces, the *trans*-acting arginine fingers are positioned too far away to interact with the
251 γ-phosphate of ATP (*e.g.*, ~9 Å for R184 of RFC2, ~10 Å for R168 of RFC5, and ~7 Å for
252 R193 of RFC4) (Fig 4c). Prior research has indicated that hydrolysis at the large
253 subunit/RFC2 interface is not essential for clamp loading by various loaders (48-51), while
254 the others are critical for the clamp-loading activity of eukaryotic RFCs.

255 In CTF18-RFC, the AAA+ spiral is overtwisted in a manner reminiscent of the
256 autoinhibited conformations observed in hRFC and scRFC (8, 10) (Fig 1d), leading to
257 steric hindrance that impedes DNA binding (Fig 4b). Specifically, the overtwisted RFC3
258 and RFC4 subunits occupy the space normally filled by DNA. In the autoinhibited
259 structure of hRFC, the β-hairpin (residues 68-88) located at the base of RFC3 also
260 referred to as "E-plug", extends towards the anticipated location of DNA and interacts with
261 the Rossmann fold of RFC1 (10). Conversely, in CTF18-RFC, while this same β-hairpin
262 is oriented toward the interior of the DNA-binding channel (Fig 4d), it does not make direct
263 contact with the Ctf18 subunit. Collectively, the E-plug appears a conserved feature in
264 eukaryotic clamp loaders, underlying its importance in maintaining the pentamer in its
265 autoinhibited conformation, by preventing DNA access through the central channel. We
266 observed that human CTF18-RFC shares an additional structural feature with both human
267 and yeast RFC: the presence of a separation pin in the large subunit (10, 11). Although
268 the separation pin is not essential for clamp loading (11), its conservation across species
269 and clamp loader types suggests an auxiliary or context-dependent function. Interestingly,
270 residues W638 and F582—proposed to stabilize the separation pin and its interaction

271 with DNA in yeast RFC—are substituted by F692 and H645 in human CTF18-RFC,
272 respectively (Fig 4e), possibly indicating a mechanistically similar role in both systems.
273 To discount the possibility that the absence of the Mg^{2+} ions in the cryo-EM sample
274 could have hindered the proper assembly of the CTF18-RFCpentamer for DNA
275 engagement, we used cryo-EM to visualize CTF18-RFC with PCNA, primer-template
276 DNA, ATP, and Mg^{2+} (Fig S6-7, S1 Table). Despite the inclusion of Mg^{2+}, the resulting 3.2
277 Å reconstruction of the complex remained in a configuration analogous to that without
278 Mg^{2+} (Fig 5a-b, Fig S6). In this reconstruction, distinct density for Mg^{2+} is noted in the
279 active sites of RFC2 and RFC5, coordinating ATP (Fig 5b). Similar to the map without
280 Mg^{2+}, ADP coordination is present in RFC3, while RFC4 is not engaged with any
281 nucleotide. These findings collectively imply that the presence of Mg^{2+} in the nucleotide
282 binding sites does not influence the transition of CTF18-RFC from an autoinhibited to an
283 active state. This result also confirms the remarkable stability of the autoinhibited
284 conformation, even in hydrolysing conditions.
285

286 The Ctf18 β-hairpin plays a role in PCNA loading and in
287 stimulating DNA synthesis by Pol ε

288 Based on the structures reported herein, the β-hairpin at the disordered N-terminal
289 domain of Ctf18 is a distinctive feature that may serve to stabilize the CTF18-RFC
290 pentamer and maximize its clamp loading efficiency. To investigate the functional
291 importance of the β-hairpin, we purified a CTF18-RFC mutant with a truncation at the
292 disordered N-terminal domain of the Ctf18 subunit, specifically, the segment spanning
293 residues 165-194 ($CTF18^{\Delta 165\text{-}194}$-RFC). This mutation eliminates the entire Ctf18 β-

294 hairpin and is expected to destabilize the CTF18-RFC pentamer. In agreement, when
295 mutant CTF18-RFC was imaged by cryo-EM with PCNA in the same conditions used for
296 wild type CTF18-RFC, only a small subset of particles of the complex was observed, while
297 the majority of particles contained dissociated PCNA (Fig S8-9). We hypothesized that
298 this destabilizing mutation in CTF18-RFC may reduce its efficiency in loading PCNA onto
299 DNA.

300 To test this, and to directly compare CTF18-RFC activity to the canonical clamp
301 loader RFC, we used a pre-steady state ensemble FRET assay to monitor loading of Cy5-
302 labeled PCNA onto a Cy3-labeled primer-template DNA substrate pre-coated with RPA
303 (Fig 6 and Fig S10). Upon addition of RFC, CTF18-RFC, or the mutant CTF18 $^{\Delta 165\text{-}194}$ -
304 RFC complex, a time-resolved increase in FRET signal was observed, corresponding to
305 productive PCNA loading. While both CTF18 and CTF18$^{\Delta 165\text{-}194}$ -RFC were able to load
306 PCNA onto DNA, the loading kinetics differed significantly: CTF18-RFC displayed a
307 slightly faster rate than RFC, whereas CTF18$^{\Delta 165\text{-}194}$-RFC exhibited a >2-fold reduction in
308 the fast-phase rate constant (k_1), consistent with a functional defect (Table 1). Importantly,
309 the FRET amplitude was comparable between the two CTF18-RFC isoforms, indicating
310 that the mutation does not prevent PCNA loading per se but affects the rate at which
311 loading occurs. These results suggest that the β-hairpin contributes to the efficiency—but
312 not the capacity—of PCNA loading by CTF18-RFC.

313 We then tested whether the observed loading defect observed with CTF18$^{\Delta 165\text{-}194}$
314 -RFC results in diminished stimulation of primer synthesis by Pol ε. To test this hypothesis,
315 we performed primer extension assays using Pol ε, PCNA, and either wild-type or mutant
316 CTF18-RFC constructs to assess their ability to stimulate DNA synthesis by Pol ε. Our

317 results indicate a significant reduction in primer extension products when the β-hairpin
318 was deleted (Fig 7a). Measurement of band intensities revealed an approximately two-
319 fold decrease in the amount of extended primer produced by the mutant compared to the
320 wild-type (Fig 7b). To further support that the observed effect on primer extension is due
321 to the mutation, we conducted a concentration titration comparing wild-type and mutant
322 CTF18-RFC (Fig S11). The CTF18-RFC mutant displayed altered concentration
323 dependencies compared to the wild-type, thereby validating the mutant phenotype and
324 underscoring the structural importance of the β-hairpin feature. Notably, the primer
325 extension assay was conducted with 2 nM plasmid DNA and excess CTF18-RFC (40 nM),
326 PCNA (100 nM), and Pol ε (30 nM), establishing single-turnover conditions per DNA
327 molecule. Under these conditions, the rate—not the extent—of PCNA loading becomes
328 the key determinant of synthesis dynamics. Although Pol ε can initiate synthesis
329 independently of PCNA, the clamp is required for full processivity. Therefore, the >2-fold
330 slower loading rate observed for the CTF18-RFC mutant likely delays formation of highly
331 processive complexes, resulting in a slower accumulation of extended products and
332 explaining the observed ~2-fold reduction in synthesis.
333

334 Discussion

335 In this work, we reported the structure of the human CTF18-RFC clamp loader bound to
336 PCNA in the presence of ATP with or without Mg^{2+} ions. Our cryo-EM data, together with
337 previous work (34, 37), support that the Ctf8 and Dcc1 subunits of CTF18-RFC, forming
338 the regulatory module interacting with Pol ε (37), are flexibly tethered to the RFC-module
339 via binding to the Ctf18 C-terminus, which is separated by the N-terminal RFC1-like

340 module of Ctf18 by ~90 amino acid flexible linker. Therefore, CTF18-RFCcomprises two
341 structurally distinct modules that cooperate to load PCNA onto the leading strand,
342 facilitating replication by Pol ε.

343 The CTF18-RFC–PCNA complex was observed in an autoinhibited conformation,
344 which prevents DNA binding. This mirrors the similar conformation in hRFC and scRFC,
345 as previously reported (10, 11). Such conformation represents a transient encounter
346 complex that occurs early in the clamp loading process, before the opening of the clamp.
347 Despite the variations in the large RFC subunit in the two assemblies, we demonstrate a
348 striking architectural conservation between the alternative human clamp loader CTF18-
349 RFCand the canonical RFC. Specifically, CTF18-RFC utilizes four subunits (Ctf18, RFC2,
350 RFC5, and RFC4) to engage two PCNA protomers. However, the engagement of the third
351 PCNA protomer by RFC3 is necessary to initiate the opening of the PCNA ring interface,
352 a process that requires a conformational shift of the AAA+ pentamer from an autoinhibited
353 to an active state. Supporting this, previous structural studies on scRFC have shown that
354 the conformation of RFC bound to open PCNA is facilitated through a 'crab-claw'
355 mechanism, which is inherently predisposed to DNA binding (11). This conformational
356 change creates an opening between the A′ segment and the AAA+ module in the A
357 subunit, allowing primer-template DNA to bind within the RFC inner chamber (11) (Fig
358 4C). Remarkably, this significant conformational shift occurs rapidly (52), does not depend
359 on ATP hydrolysis, and ensures the sequential binding of PCNA and the DNA substrate
360 in the correct order. While our study did not resolve the active conformation of CTF18-
361 RFC, the observed structural conservation in the autoinhibited state, particularly of the
362 large Ctf18 subunit (Fig 2), suggests that a similar 'crab-claw' mechanism may facilitate

363 the transition of CTF18-RFC to its active state for PCNA opening and DNA binding. While
364 our work was being finalized, several cryo-EM structures of human CTF18-RFC bound to
365 PCNA, and primer/template DNA were reported by another group (53). These findings
366 are consistent with the distinct features of CTF18-RFC observed in our structures and
367 independently support the notion of significant mechanistic similarity between CTF18-
368 RFC and canonical RFC in loading PCNA onto a ss/dsDNA junction.

369 The main structural differences between CTF18-RFC and the canonical RFC
370 include increased mobility of the large subunit and the presence of a β-hairpin that
371 attaches to the RFC5 subunit. The mobility of the large subunit is likely enhanced by the
372 low-affinity PIP motif that anchors it to the PCNA ring. We propose that the β-hairpin may
373 have evolved to counterbalance the mobility of the large subunit, helping to maintain its
374 connection to the RFC pentamer and stabilizing the clamp loader structure. Our structural
375 data and functional assays indeed show that deletion of the β-hairpin results in reduced
376 stability of the CTF18-RFC–PCNA complex, slower clamp loading activity, and diminished
377 activity of CTF18-RFC in stimulating Pol ε primer synthesis, likely due to reduced CTF18-
378 RFC efficiency in PCNA loading (Fig 8). Interestingly, a recent work reporting cryo-EM
379 structures of the yeast homolog of CTF18-RFC bound to PCNA (54) does not support the
380 presence of a stable β-hairpin at the N-terminus of the Ctf18 subunit engaged to the collar
381 of the Rfc3 subunit. Therefore, the functional β-hairpin we observed in human CTF18-
382 RFC appears a distinct feature that pertains to higher eukaryotes, required to maximize
383 the activity of CTF18-RFC in loading PCNA onto the leading strand.

384

385 # Materials and Methods

386 # Protein expression and purification

387 ## Preparation of CTF18-RFC

388 MultiBac™ expression system (Geneva Biotech) was used to express human Ctf18-
389 RFC2-5 along with two additional cohesion-specific factors, Dcc1 and Ctf8 (named
390 hereafter CTF18-RFC) in Sf9 insect cells. For this purpose, insect cells optimized
391 sequences of N-terminus twin Strept-tagged TEV Ctf18, RFC2, and RFC4 were cloned
392 in pACEBac1 plasmid with independent promoters and terminators, and N-terminus 6X
393 histidine-tagged RFC3, RFC5, Dcc1 and Ctf8 were cloned in pIDS plasmid with
394 independent promoters and terminators by GenScript. Finally, the single transfer vector
395 with different subunit assemblies was generated using *cre* recombinase according to the
396 MultiBac™ expression system user manual. CTF18-RFC encoding all seven subunits in
397 a single MultiBac™ expression plasmid (pACEBac1) was transformed into
398 DH10MultiBac™ cells to make bacmid DNA. To prepare the baculovirus, bacmid DNA
399 containing all subunits was transfected into Sf9 cells using FuGENE® HD (Promega)
400 according to the manufacturer's instructions. This baculovirus prep was amplified twice
401 to obtain a higher titer virus (P3 virus). The expression of CTF18-RFC then proceeded by
402 transfecting a 6 L Hi5 suspension culture at a density of 2×10^6 cells/mL with the P3 virus
403 for 60-65 hours.

404 Cells were collected by centrifugation at 5,500 xg for 10 minutes and re-suspended in
405 lysis buffer [50 mM Tris-HCl (pH 7.5), 300 mM NaCl, 20 mM imidazole, 5 mM BME, 0.1%
406 Nonidet P-40, 10% glycerol and one EDTA-free protease inhibitor cocktail tablet/50 mL].
407 All further steps were performed at 4° C. Cells were sonicated and debris was removed
408 by centrifugation at 95,834 xg for 1 hour at 4 °C. The resultant supernatant was directly

409 loaded onto a HisTrap HP 5 mL affinity column (Cytiva) pre-equilibrated with buffer A [50
410 mM Tris-HCl (pH 7.5), 300 mM NaCl, 20 mM imidazole, 5 mM BME and 10% glycerol].
411 After loading, the column was washed with 50 mL of buffer A and the bound fractions
412 were eluted by gradient with 50 mL of buffer B [50 mM Tris-HCl (pH 7.5), 300 mM NaCl,
413 500 mM imidazole, 5 mM BME, and 10% glycerol]. The eluents were pooled and directly
414 loaded onto Strept Trap XT 1 mL affinity column pre-equilibrated with buffer A [50 mM
415 Tris-HCl (pH 7.5), 300 mM NaCl, 5 mM BME and 10% glycerol]. After loading, the column
416 was washed with 10 mL of buffer A, followed by step elution with buffer B [50 mM Tris-
417 HCl (pH 7.5), 300 mM NaCl, 50 mM Biotin, 5 mM BME, and 10% glycerol]. Eluents were
418 pooled and incubated with the TEV protease overnight. Fractions were concentrated to 1
419 mL and loaded onto HiLoad 16/600 Superdex 200 pg pre-equilibrated with gel filtration
420 buffer [50 mM Tris-HCl (pH 7.5), 200 mM NaCl, 1 mM DTT, and 10% glycerol]. Protein
421 fractions were pooled in a total volume of 1.6 mL, flash frozen, and stored at -80°C.
422

423 **Preparation of PCNA**

424 To express PCNA BL21(DE3) *E. coli* cells were transformed with WT PCNA plasmid. The
425 transformed cells were grown at 37°C in 2YT media supplemented with ampicillin to an
426 OD600 of 1.2. The cell cultures were induced with 0.5 mM isopropyl-beta-D-1-
427 thiogalactopyranoside (IPTG) and let them grow for 19 hours at 16°C. Cells were then
428 harvested by centrifugation at 5500 xg for 10 minutes and then re-suspended in lysis
429 buffer [50 mM Tris-HCl (pH 7.5), 750 mM NaCl, 20 mM imidazole, 5 mM BME, 0.2%
430 Nonidet P-40, 1 mM PMSF, 5% glycerol and one EDTA-free protease inhibitor cocktail
431 tablet/50 mL]. The cells were lysed with 2 mg/mL of lysozyme at 4°C for 30 minutes. Cells

432 were sonicated and debris was removed by centrifugation at 22,040 xg for 20 minutes at
433 4°C. The cleared cell lysate was directly loaded onto a HisTrap HP 5 mL affinity column
434 (Cytiva) pre-equilibrated with buffer A [50 mM Tris-HCl (pH 7.5), 500 mM NaCl, 20 mM
435 imidazole, 5 mM BME and 5% glycerol]. The column was firstly washed with 50 mL of
436 buffer A and then with 50 mL of buffer B containing low salt [50 mM Tris-HCl (pH 7.5), 100
437 mM NaCl, 500 mM imidazole, 5 mM BME, and 5% glycerol]. The eluents were pooled
438 and directly loaded onto HiTrap Q HP 5 mL anion exchange column (GE Healthcare) pre-
439 equilibrated with buffer D [50 mM Tris-HCl (pH 7.5), 100 mM NaCl, 5 mM BME and 5%
440 glycerol]. The column was washed with 50 mL of buffer D after loading, followed by elution
441 of 50 mL gradient with buffer E [50 mM Tris-HCl (pH 7.5), 1 M NaCl, 5 mM BME, and 5%
442 glycerol]. Eluents were pooled and concentrated to 1.5 mL and loaded onto HiLoad
443 16/600 Superdex 200 pg pre-equilibrated with gel filtration buffer [50 mM Tris-HCl (pH
444 7.5), 150 mM NaCl, 1 mM DTT, and 5% glycerol]. Protein fractions were pooled, flash-
445 frozen, and stored at -80 °C. Human RPA, Cy5-PCNA, and RFC for the clamp loading
446 assay were obtained as previously described (55, 56). The concentration of active RPA
447 was determined via a FRET-based activity assay as described previously (57).
448

449 **Preparation of DNA polymerase ε**

450 MultiBac™ expression system (Geneva Biotech) was used to express human DNA Pol ε
451 in Sf9 insect cells. For this purpose, insect cells optimized sequence of the catalytic
452 subunit, p261 was cloned in pACEBac1 and p59, C-terminus TEV twin Strept-tagged p17,
453 and N-terminus 8X histidine-tagged TEV p12 along with independent promoters and
454 terminators were cloned in pIDS by the GenScript. Finally, the single transfer vector with

455 different subunit assemblies was generated using *cre* recombinase according to
456 MultiBac™ expression system user manual. To prepare the baculovirus, the bacmid DNA
457 of Pol ε was transfected into Sf9 cells using FuGENE® HD (Promega) according to the
458 manufacturer's instructions. The resulting supernatant was obtained as the P1 virus stock
459 which was then amplified to obtain P2 virus stock. P2 virus stock was then further
460 amplified to obtain P3 virus stock for large-scale expression. Pol ε was expressed by
461 transfecting 4 L of Sf9 suspension culture at 2×10^6 cells/mL density with P3 virus. Cells
462 were harvested after 72 hours by centrifugation at 5,500 xg for 10 minutes and re-
463 suspended in 200 mL of lysis buffer [50 mM HEPES (pH 8), 20 mM Imidazole, 400 mM
464 NaCl, 5 mM β-Mercaptoethanol, 5% (v/v) Glycerol, 0.1% NP-40, 1 mM PMSF and EDTA-
465 free protease inhibitor cocktail tablet/50 mL (Roche, UK)]. Cells were sonicated and debris
466 was removed by centrifugation at 95,834 xg for 1 hour at 4 °C. The resultant supernatant
467 was directly loaded onto a HisTrap HP 5 mL affinity column (Cytiva) equilibrated with
468 buffer A [50 mM HEPES (pH 8), 20 mM Imidazole, 400 mM NaCl, 5mM β-
469 Mercaptoethanol, 5% (v/v) Glycerol and EDTA-free protease inhibitor cocktail tablet/50
470 mL (Roche, UK]. After loading, the column was washed with 50 mL of buffer A and the
471 bound fractions were eluted by gradient with 50 mL of buffer B [50 mM HEPES (pH 8),
472 500 mM Imidazole, 300 mM NaCl, 5 mM β-Mercaptoethanol, 5% (v/v) Glycerol and EDTA-
473 free protease inhibitor cocktail tablet/50 ml (Roche, UK)]. Peak fractions containing Pol ε
474 subunits were pooled and loaded directly onto Strep Trap XT 5 mL (Cytiva) column
475 equilibrated with buffer C [50 mM HEPES (pH 8), 250 mM NaCl, 5 mM β-
476 Mercaptoethanol, 5% (v/v) Glycerol] and EDTA-free protease inhibitor cocktail tablet/50
477 mL (Roche, UK)]. After loading, the column was washed with 50 mL of buffer C and the

478 bound fractions were incubated for 2-4 hours with 15 mL of 100% buffer D [50 mM HEPES
479 (pH 8), 100 mM NaCl, 50 mM Biotin, 5 mM β-Mercaptoethanol, 5% (v/v) Glycerol] and
480 EDTA-free protease inhibitor cocktail tablet/50 mL (Roche, UK)] and eluted further with
481 30 mL of 100% buffer D. Fractions that contain all Pol ε subunits were pooled and
482 incubated with the TEV protease for overnight and loaded onto an anion exchanger, Mono
483 Q 5/50 GL column (Cytiva) pre-equilibrated with buffer E [50 mM HEPES (pH 8), 100 mM
484 NaCl, 5 mM β-Mercaptoethanol and 5% Glycerol]. After loading, the column was washed
485 with 15 mL of buffer E. The Pol ε was eluted with a 10 mL gradient from 100 mM NaCl to
486 1 M NaCl in 50 mM HEPES (pH 8), 5 mM β-Mercaptoethanol, and 5% Glycerol. The
487 fractions that contained all Pol ε subunits were combined and concentrated to 1 mL and
488 loaded onto HiLoad 16/600 Superdex 200 pg (Cytiva) pre-equilibrated with gel filtration
489 buffer [50mM HEPES (8), 200 mM NaCl, 1 mM DTT and 5% Glycerol]. Protein fractions
490 were pooled, flash-frozen, and stored at −80°C.
491
492 All protein concentrations were calculated by measuring their absorbance at 280 nm
493 using the extinction coefficients calculated from the amino acid composition (CTF18-RFC:
494 216,360 M^{-1} cm^{-1}; PCNA: 47,790 M^{-1} cm^{-1}, Pol ε: 351,470 M^{-1} cm^{-1}).
495

496 ## DNA substrates for Cryo-EM

497 For the primer/template substrates used in all the structures described here, 80 base pairs
498 template strand 5'-TTTTTTTTTTTTTTTTTTTTTTTTTTTTTTTTTTTTTTTTTTTTGACTGCAC
499 GAATTAAGCAATTCGTAATCATGG TCATAGCT-3' was annealed to a 39 base pairs
500 primer containing a 3' dideoxy cytosine chain terminator 5'-AGCTATG

501 ACCATGATTACGAATTGCTTAATTCGTGCAGT[ddC]-3' to form the P/T substrate. The
502 strands were mixed in an equimolar ratio in the presence of 20 mM Tris pH 7.5 and 25
503 mM NaCl. The annealing reaction was performed by incubating the P/T at 92°C for 2
504 minutes followed by slow cooling to room temperature overnight. All oligonucleotides were
505 purchased from IDT Integrated DNA Technologies.

506 Clamp loading and primer extension substrates

507 Oligonucleotides for the clamp loading assay comprising the 5′ddPCy3/T P/T DNA
508 substrate were synthesized by Integrated DNA Technologies (Coralville, IA) and purified
509 on denaturing polyacrylamide gels. The concentration of unlabeled template strand DNA
510 was determined from the absorbance at 260 nm using the provided extinction coefficient.
511 Concentrations of the Cy3-labeled primer strand DNA was determined from the extinction
512 coefficient of Cy3 at 550 nm (ε_{550} = 136,000 $M^{-1}cm^{-1}$). For annealing the 5′ddPCy3/T P/T
513 DNA substrate, the Cy3-labled primer strand DNA and the unlabeled template strand DNA
514 were mixed in equimolar amounts in 1X annealing buffer (10 mM TrisHCl, pH 8.0, 100
515 mM NaCl, 1 mM EDTA), heated to 95 ^{o}C for 5 minutes, and allowed to slowly cool to room
516 temperature. For the prime extension assay, Oligo
517 (592:TAACGCCAGGGTTTTCCCAGTCACG) (Integrated DNA Technologies) was
518 annealed to 50 nM M13mp18 single-stranded DNA (New England Biolabs) in a reaction
519 buffer consisting of [10 mM Tris-HCl (pH 7.6), 100 mM NaCl and 5 mM EDTA]. The
520 mixture was heated to 95 °C for 5 minutes, then cooled gradually to room temperature.
521 The unannealed oligonucleotide was removed using a QIAquick PCR purification kit
522 (Qiagen).
523

524 ## Pre-steady state FRET measurements

525 All experiments were performed at room temperature (23 ± 2 °C) in a 16.100F-Q-10/Z15
526 sub-micro fluorometer cell (Starna Cells) and monitored in a Horiba Scientific Duetta-Bio
527 fluorescence/absorbance spectrometer as described previously (57). In short, reaction
528 solutions are excited at 514 nm and the fluorescence emission intensities (*I*) are
529 monitored essentially simultaneously (Δt = 0.118 ms) at the peak emission wavelengths
530 for Cy3 (563 nm, I_{563}) and Cy5 (665 nm, I_{665}) over time, recording *I* every 0.17 s. For all
531 experiments, excitation and emission slit widths are 10 nm. All recorded fluorescence
532 emission intensities are corrected by a respective dilution factor and all-time courses are
533 adjusted for the time between the addition of each component and the fluorescence
534 emission intensity recordings (i.e., dead time = 6 s). For any recording of the fluorescence
535 emission intensities (I_{665} and I_{563}), the approximate FRET efficiency is estimated from the
536 equation $E_{FRET} = \frac{I_{665}}{I_{665}+I_{563}}$. For each experiment below, the final concentrations of all
537 reaction components are indicated.

538 PCNA loading experiments were carried out in 1X Replication Buffer (25 mM HEPES, pH
539 7.5, 125 mM KOAc, 10 mM $Mg(OAc)_2$) supplemented with 1 mM DTT, 1 mM ATP, and the
540 ionic strength adjusted to physiological (200 mM) by addition of KOAc. Experiments were
541 performed via slight modifications to a published protocol (58, 59). In short, 5′ddPCy3/T
542 P/T DNA (200 nM, NeutrAvidin (800 nM homotetramer), and ATP (1 mM) are pre-
543 incubated with RPA (600 nM heterotrimer). Then, Cy5-PCNA (200 nM homotrimer) is
544 added, the resultant solution is transferred to a fluorometer cell, and the cell is placed in
545 the instrument. I_{665} and I_{563} are monitored until both stabilize for at least 1 min. The E_{FRET}
546 values within this stable region represent the signal for Cy5-PCNA remaining completely

547 disengaged from 5¢ddPCy3/T•RPA nucleoprotein complex and are averaged to obtain
548 the E_{FRET} value observed prior to addition of a clamp loader complex. Finally, a clamp
549 loader complex (200 nM RFC, CTF18, or CTF18$^{\Delta 165\text{-}194}$ -RFC heteropentamer) is added,
550 the resultant solution is mixed, and I_{665} and I_{563} are monitored, beginning 6 s after the
551 addition of the respective clamp loader complex (i.e., Δt = 6 s).

552 Primer extension assay

553 The primer extension reaction was conducted in a reaction buffer containing [40 mM
554 HEPES (pH 7.6), 100 mM K-glutamate, 1 mM DTT, 10 mM Mg-Acetate, 200 µg/mL BSA,
555 1 mM ATP, 100 µM each of dATP, dTTP, and dGTP, 20 µM dCTP, and 10 µCi of [^{32}P]-
556 dCTP (Hartmann)]. Two nanomolar of the primed-M13 template were initially incubated
557 at 37 °C for 10 minutes with 100 nM PCNA, 400 nM RPA, and either CTF18-RFCWT
558 or CTF18$^{\Delta 165\text{-}194}$-RFC. The reaction was initiated by the addition of 30 nM Pol ε. Reactions
559 were stopped at the indicated time point by adding 50 mM EDTA and electrophoresed on
560 0.7% alkaline agarose gel at 35 V for 17 hours. The gel was backed with DE81 paper,
561 compressed, and imaged in a Sapphire Biomolecular Imager (Azure Biosystems). All the
562 experiments were performed in triplicate.
563

564 Cryo-EM grids preparation and data collection

565 For all the complexes (WT and mutant), UltraAuFoil® R1.2/1.3 Au 300 grids were glow-
566 discharged at 30 mA for 30 seconds on an EasyGlow glow-discharge unit. For the
567 preparation of the complex without Mg^{2+} **(Dataset 1 and Dataset 3)**, P/T DNA, ATP,
568 CTF18-RFC WT/CTF18$^{\Delta 165\text{-}194}$-RFC, and PCNA were mixed in order. The final
569 concentrations were 5.6 µM P/T DNA, 0.2 mM ATP, 1.5 µM CTF18-RFC WT/CTF18$^{\Delta 165\text{-}}$

570 ^{194}-RFC, and 7.5 μM PCNA. The buffer this was performed in comprised 50 mM Tris-HCl
571 pH 7.5, 200 mM NaCl, 1 mM DTT, and 0.5 mM ATP. 3 μL of the sample was applied to
572 the grid, blotted for 2 s at blot force -5, and plunged frozen into liquid ethane using a
573 Vitrobot Mark IV (FEI Thermo Fisher), which was set at 4°C and 100% humidity. For the
574 preparation of CTF18-RFC/PCNA/P-T DNA/ATP/Mg^{2+}complex **(Dataset 2)**, the
575 components P/T DNA, ATP, Mg^{2+}, CTF18-RFC, and PCNA were mixed in order. The final
576 concentrations were 5.6 μM P/T DNA, 0.2 mM ATP, 1.9 mg/mL Mg^{2+}, 1.5 μM CTF18-RFC,
577 and 7.5 μM PCNA. The buffer this was performed in comprised 50 mM Tris-HCl pH 7.5,
578 200 mM NaCl, 1 mM DTT, 0.5 mM ATP, and 5 mM Mg^{2+}. 3 μL of the sample was applied
579 to the grid in the same way as above for data collection. Cryo-EM data for all the samples
580 were collected on a Thermo Fisher Scientific Titan Krios G4 transmission electron
581 microscope at KAUST. Electron micrographs for **Dataset 1** (CTF18-RFC-PCNA with ATP
582 in the absence of Mg^{2+}), were collected using a Falcon 4i detector at a dose rate of 7.5 e^-
583 /pix/sec for 5 seconds and a calibrated pixel size of 0.93 Å. Focusing was performed over
584 a range between -2.7 μm and -1.5μm, in 0.3 μm intervals. Electron micrographs for
585 **Dataset 2** (CTF18-RFC-PCNA with ATP and Mg^{2+}) were collected using a Falcon 4i
586 detector at a dose rate of 8.02 e^-/pix/sec for 5 seconds and a calibrated pixel size of 0.93
587 Å. Focusing was performed over a range between -2.7 μm and -1.5 μm, in 0.3 μm
588 intervals. Electron micrographs for **Dataset 3** (CTF18$^{\Delta 165\text{-}194}$-RFC-PCNA with ATP and in
589 the absence of Mg^{2+}) were collected using a Falcon 4i detector at a dose rate of 7.4 e^-
590 /pix/sec for 5 seconds and a calibrated pixel size of 0.93 Å. Focusing was performed over
591 a range between -2.7 μm and -1.5 μm, in 0.3 μm intervals.
592

593 ## Cryo-EM image processing

594 Preprocessing of all datasets (**Dataset 1**: CTF18-RFC, ATP, primer/template DNA and
595 PCNA; **Dataset 2:** CTF18-RFC, ATP, Mg^{2+}, primer/template DNA and PCNA; **Dataset 3**:
596 $CTF18^{\Delta 165-194}$-RFC, ATP, primer/template DNA and PCNA) was performed as follows: the
597 micrographs were corrected for beam-induced motion and then integrated using
598 MotionCor2 (60). All frames were retained and a patch alignment of 4x4 was used.
599 CTFFIND-4.12 estimated Contrast Transfer Function (CTF) parameters for each
600 micrograph (61). Integrated movies were inspected with Relion-4.0 (**Dataset 1** and
601 **Dataset 2**) and Relion-5.0 (**Dataset 3**) for further image processing (7906 movies for
602 **Dataset 1**, 6181 movies for **Dataset 2**, and 6499 movies for **Dataset 3**) (62). Particle
603 picking was performed in automated mode using Topaz (63) for **Dataset 1**. Particle
604 extraction was carried out from micrographs using a box size of 55 pixels (pixel size: 3.65
605 Å/pixel). An initial dataset of 2 x 10^6 particles was cleaned by 2D classification followed
606 by 3D classification with alignment. Three 3D classes were generated with populations of
607 31, 28, and 40%. 3D refinement, CtfRefine, and polishing were performed on the selected
608 3D classes corresponding to populations 31 and 40%. A bigger box size, 480 pixels (pixel
609 size: 0.93 Å/pixel) was used to re-extract the particles. 3D refinement, CtfRefine, and
610 polishing yielded reconstruction at 2.9 Å.

611 Particle picking was performed in reference-based mode for **Dataset 2**. Particle extraction
612 was carried out from micrographs using a box size of 55 pixels (pixel size of 3.65 Å/pixel).
613 An initial dataset of 3 x 10^6 particles was cleaned by 2D classification followed by 3D
614 classification with alignment. Three 3D classes were generated with 30, 33, and 36%
615 populations. 3D refinement, CtfRefine, and polishing were performed on the selected 3D

616 classes corresponding to populations 33 and 36%. 3D refinement, CtfRefine, and
617 polishing yielded reconstruction at 3.2 Å. Particle picking was performed in automated
618 mode using Topaz (63) for **Dataset 3**. Particle extraction was done from micrographs
619 using a box size of 220 pixels (pixel size: 0.93 Å/pixel). An initial dataset of 1 x 10^6 particles
620 was cleaned by 2D classification. For quantification of complex stability, the number of
621 particles contributing to each 2D class was extracted from the classification metadata
622 (**Datasets 1** and **3**). All classes showing isolated PCNA rings were summed and
623 compared to the total number of particles in classes representing intact CTF18-RFC–
624 PCNA complexes. This analysis was performed for both wild-type and β-hairpin deletion
625 mutant datasets. Notably, no 2D classes corresponding to free PCNA were observed in
626 the wild-type dataset, whereas in the mutant dataset, a substantial fraction of particles
627 corresponded to isolated PCNA, suggesting reduced stability of the mutant complex.
628

629 ## Cryo-EM 3D Variability Analysis

630 3DVA (43, 44) of the CTF18-RFC–PCNA consensus maps, with and without Mg^{2+}, was
631 performed in CryoSPARC v 4.6 using their respective refinement masks, employing three
632 modes and a resolution filter of 5 Å, based on global FSC resolutions of 2.9 Å and 3.2 Å,
633 respectively. For each mode, 3 frames were generated and morphed to visualize the
634 conformational flexibility across the components.
635

636 ## Molecular Modelling

637 The structure of the Ctf18 large subunit of human CTF18-RFC (Q8WVB6, residues 277-
638 805) was generated with Phyre2 (64), using as a template the sequence of human RFC1

639 (P35251, residues 581-1034). The Ctf18 subunit model was then aligned to the RFC1
640 subunit in the structure of the human RFC clamp loader bound to PCNA in an
641 autoinhibited conformation (PDB 6VVO, (10)) using Chimera, the RFC1 subunit was
642 deleted, and the resulting model including Ctf18, subunits RFC2-5 and PCNA was rigid-
643 body fitted into the cryo-EM map. The model was edited and real-space refined with Coot
644 (65) following flexible fitting performed with ISOLDE (66). A final real-space refinement
645 was performed in Phenix (67), applying secondary structure constraints. The models of
646 both CTF18-RFC–PCNA complexes with and without the Mg^{2+} ion were generated
647 similarly.
648

649 # Acknowledgments

650 This research was supported by King Abdullah University of Science and Technology
651 (KAUST) through core funding (to S.M.H. and A.D.B.). We thank Lingyun Zhao, Ashraf
652 Al-Alamoudi, Alessandro Genovese and Rachid Sougrat for their assistance at the
653 Imaging and Characterization Core Lab at KAUST. This work was also supported by
654 funding from the National Institutes of Health to M.H. (R35 GM147238-03). This
655 publication was supported, in part, by NIH Grant T32GM149417.
656

657 # Author Contributions

658 S.M.H. and A.D.B. conceived and supervised the study. M.T. and A.A. prepared proteins,
659 carried out primer extension assays and analyzed the data. G.Y. and M.H. prepared
660 proteins, carried out clamp loading assays and analyzed the data. G.R.B. and C.G.S.

661 performed cryo-EM imaging and processing. A.U.D. performed the cryo-EM 3DVA
662 analysis. G.R.B., P.Q-N., and A.D.B. performed model building and validation. A.D.B.
663 wrote the manuscript with contributions from the other authors.

664

665

666 Data Availability

667 The maps of CTF18-RFC-ATP-PCNA and CTF18-RFC-ATP-Mg^{2+}-PCNA complexes have
668 been deposited in the EMBD with accession codes EMD-60534, and EMD-60598 and the
669 atomic models in the Protein Data Bank under accession codes PDB 8ZWO and PDB
670 9IIN.

671

672 Ethics declarations

673 *Competing interests*

674 The authors declare no competing interests.

675

676

677

678

679

Figures

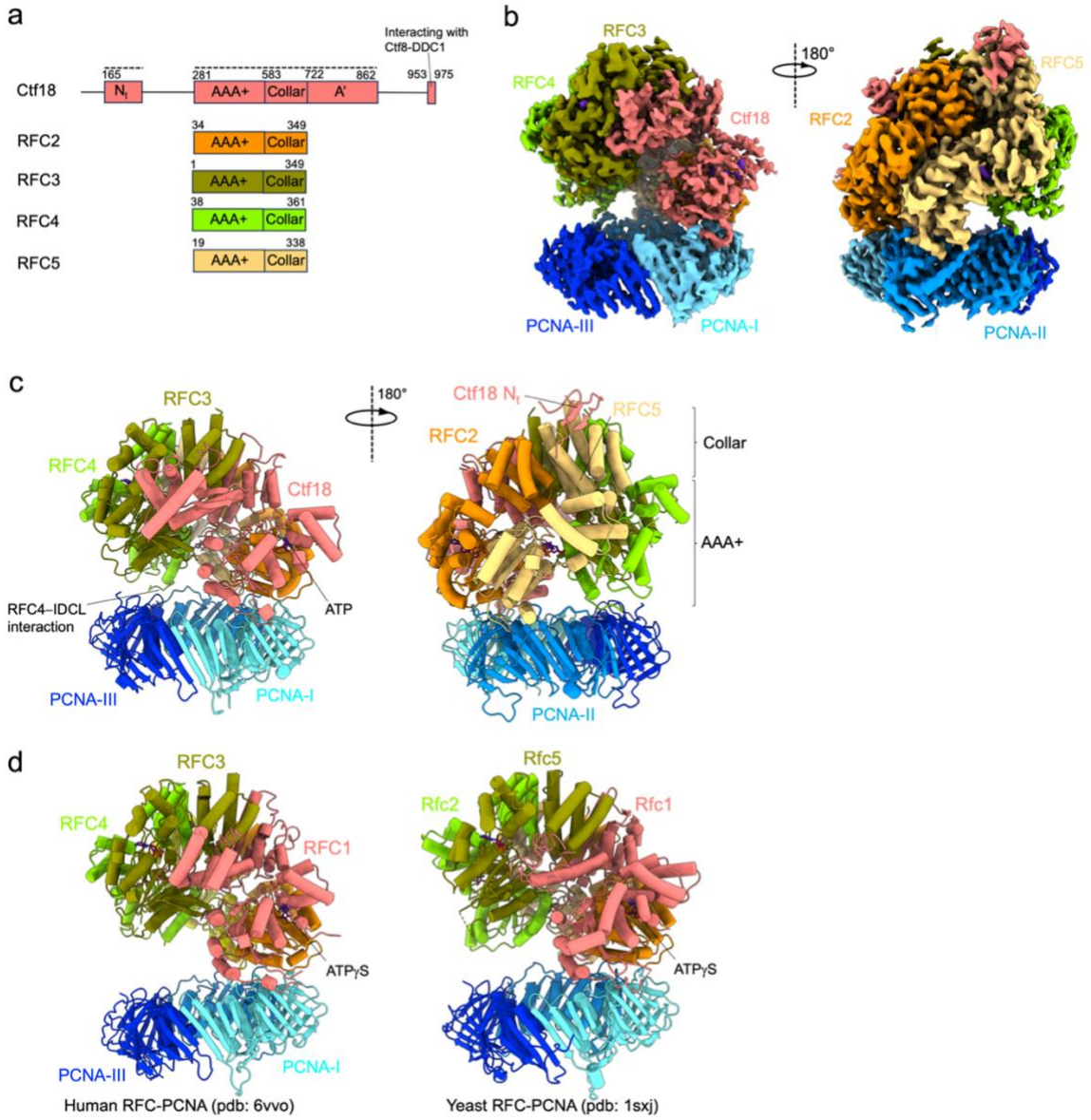

Figure 1. ***Cryo-EM structure of the human CTF18-RFC–PCNA complex in the presence of ATP.*** **a)** Domain organization of the CTF18-RFC subunits forming the RFC pentamer. The dotted line above the Ctf18 subunit highlights the regions that are observed in the cryo-EM map. **b)** Two views of the cryo-EM map of the CTF18-

686 RFC–PCNA complex, coloured by subunits. The less sharp definition of the map region
687 corresponding to the AAA+ domain of the Ctf18 subunit supports a relative high mobility
688 of this subunit. **c)** Molecular model of the CTF18-RFC–PCNA complex in ribbon
689 representation. **d)** Structures of the human (left) and *Saccharomyces cerevisiae* (right)
690 RFC–PCNA complex, which present the RFC pentamer in an auto-inhibited conformation
691 analogous to the one captured in the CTF18-RFC–PCNA complex.
692
693
694
695
696
697

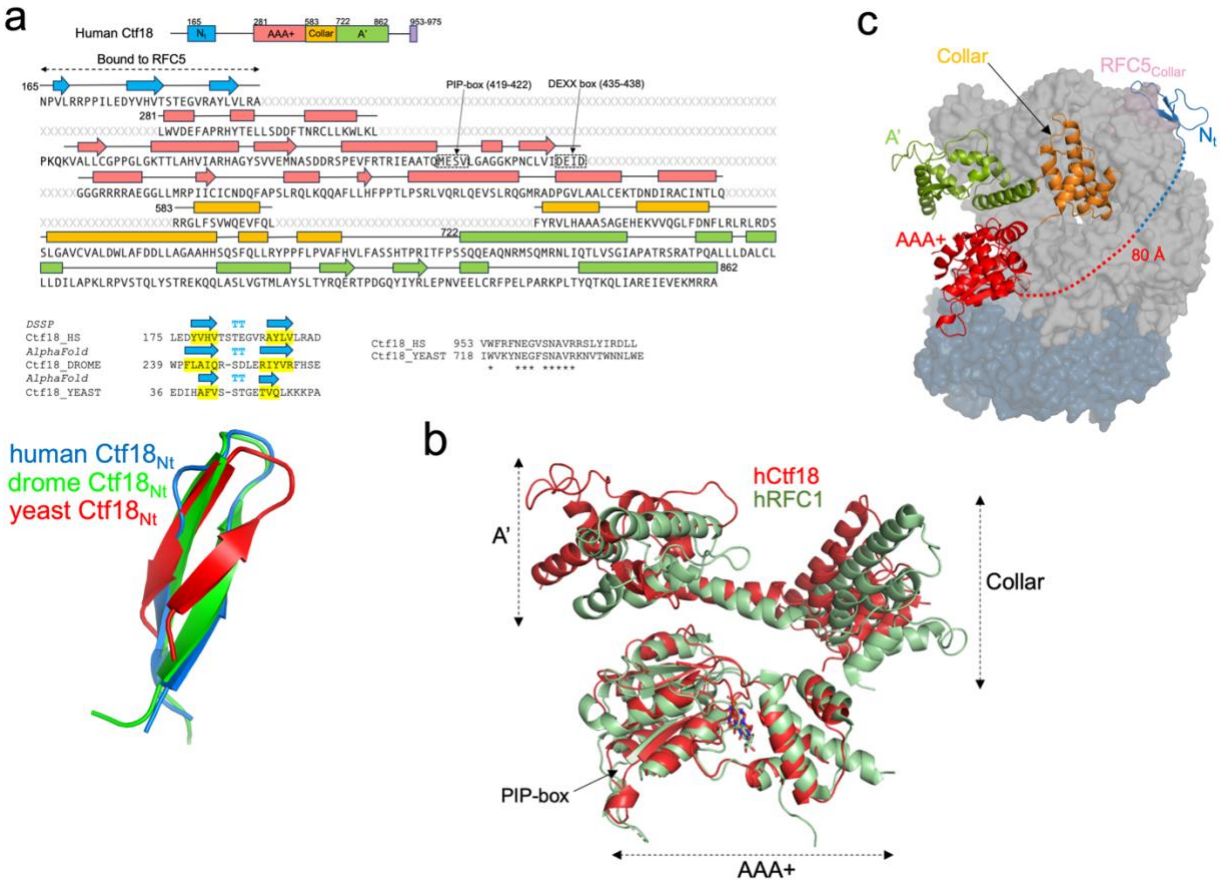

Figure 2. ***Structure of the Ctf18 subunit.*** **a)** Sequence of the human Ctf18 subunit, highlighting the secondary structural elements as assigned in the cryo-EM model. The atypical PCNA-interacting motif (PIP-box) and conserved DEXX box are boxed. Residues that are not modelled in the cryo-EM structure are labelled as X in grey. Below the Ctf18 sequence to the left, the sequences of the N-terminus of human and other lower eukaryotes Ctf18, together with the secondary prediction by AlphaFold (45) are shown, highlighting the conservation of the β-hairpin fold. Below, the cryo-EM β-hairpin fold model is overlaid onto the corresponding motifs predicted by AlphaFold for *Drosophila* or *Saccharomyces cerevisiae* Ctf18. Below the Ctf18 sequence to the right, the alignment of the C-terminal region of human and *Saccharomyces cerevisiae* Ctf18, which interacts with the Ctf8/Dcc1 subunits, is shown. Asterisks denote conserved residues. **b)**

710 Superposition of the human Ctf18 and RFC1 (PDB: 6VVO) subunit structures, with
711 subdomains labelled. **c)** Structure of the Ctf18 subunit, in ribbon representation, within
712 the CTF18-RFC–PCNA complex. The Ctf18 subdomains are coloured-coded as in panel
713 **(a)**. The other complex subunits are shown as surfaces.
714
715

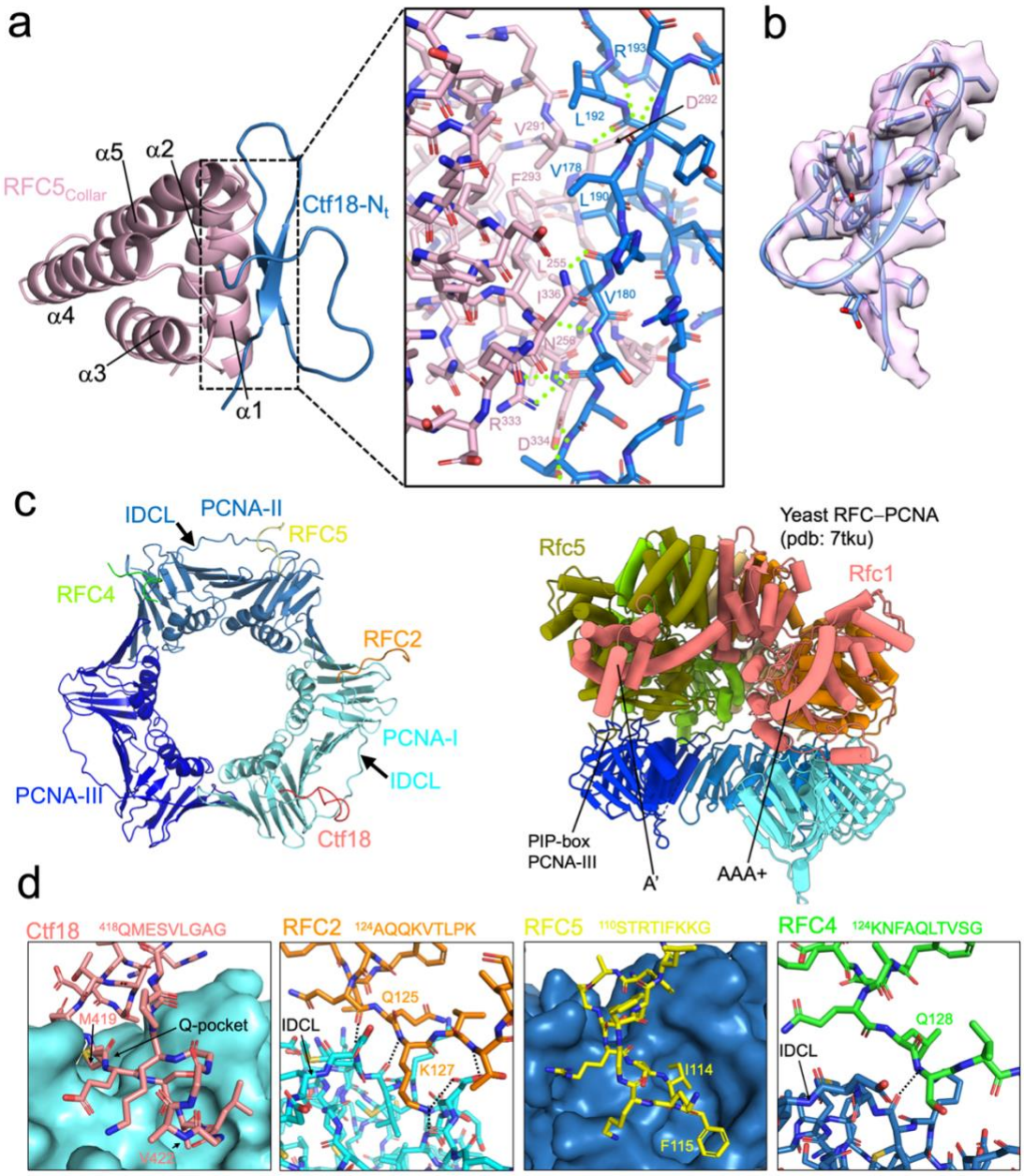

Figure 3. ***Structural details of the Ctf18–RFC5 and CTF18-RFC–PCNA interactions.*** **a)** Model of the RFC5 collar domain and Ctf18 N-terminal β-hairpin in ribbon representation. The inset shows the interface in stick representation, with hydrogen bonds shown as green dotted lines. **b)** Map region around the Ctf18 N-terminal β-hairpin. **c)** Model of the PCNA homotrimer bound to the four CTF18 interacting regions. To the right,

722 the structure of the yeast RFC–PCNA complex with an open clamp, highlighting the
723 engagement of all five RFC subunits to PCNA, required for clamp opening. **d)** Model of
724 the regions of the CTF18-RFC–PCNA interactions, with CTF18-RFC subunit residues
725 shown as sticks and PCNA as surface or ribbon. Polar interactions are shown as black
726 dotted lines. The amino acid sequence encompassing the interacting motifs in the various
727 subunits are shown.

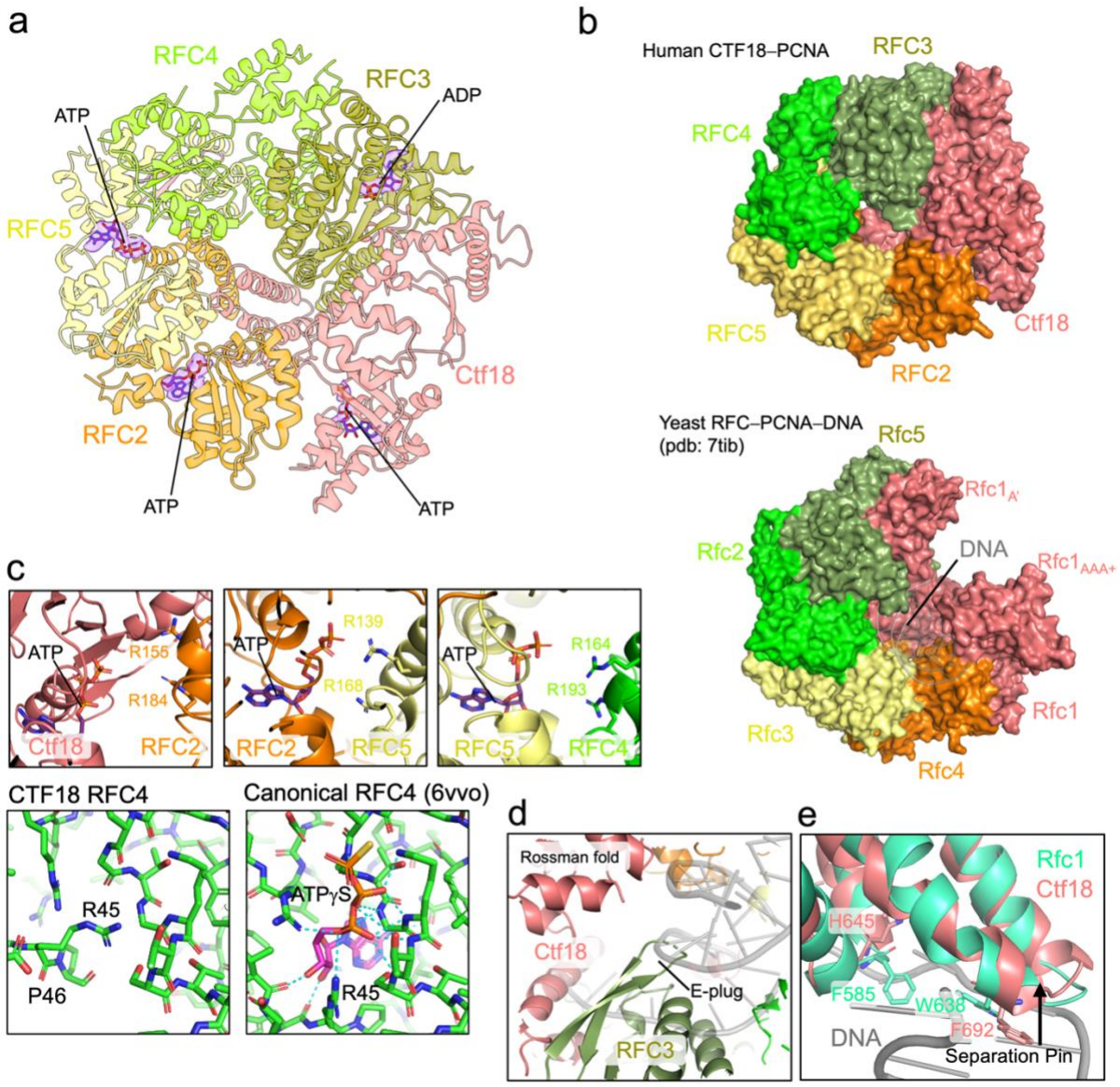

Figure 4. ***Analysis of the auto-inhibited conformation of the CTF18 pentamer and nucleotide coordination*. a)** Ribbon model of the CTF18-RFC pentamer (PCNA hidden). Nucleotide molecules are shown as sticks, with the corresponding cryo-EM density. **b)** Surface representation of (top) the CTF18-RFC pentamer and (bottom) the yeast RFC pentamer bound to open PCNA and primer-template DNA. PCNA is hidden in both structures. The overtwisted CTF18-RFC pentamer cannot accommodate DNA within the

735 inner chamber. **c)** Model of the ATP active sites in the CTF18-RFC–PCNA complex,
736 showing disruption of the interactions mediated by the arginine fingers. Below, insets
737 show the nucleotide-binding site of subunit RFC4 in either the human CTF18-RFC (left)
738 or human RFC (right) models, highlighting the structural incompatibility with nucleotide
739 binding in the CTF18-RFC structure. Polar interactions with ATPγS in human RFC4 are
740 indicated as cyan dotted lines. **d)** Detail of the inner chamber region of the CTF18-RFC
741 pentamer, showing the β-hairpin (E-plug) of RFC5 protruding in the region predicted to
742 be occupied by DNA. The DNA (grey ribbon) is modeled as in the yeast RFC–DNA–PCNA
743 complex. **e)** The structures of the RFC1 subunit from the yeast RFC–DNA–PCNA
744 complex (11) and the Ctf18 subunit from the CTF18-RFC–PCNA complex are aligned to
745 highlight conservation of the separation pin. Side chains of residues implicated in this
746 motif in yeast RFC, along with the corresponding amino acids in CTF18-RFC, are shown.

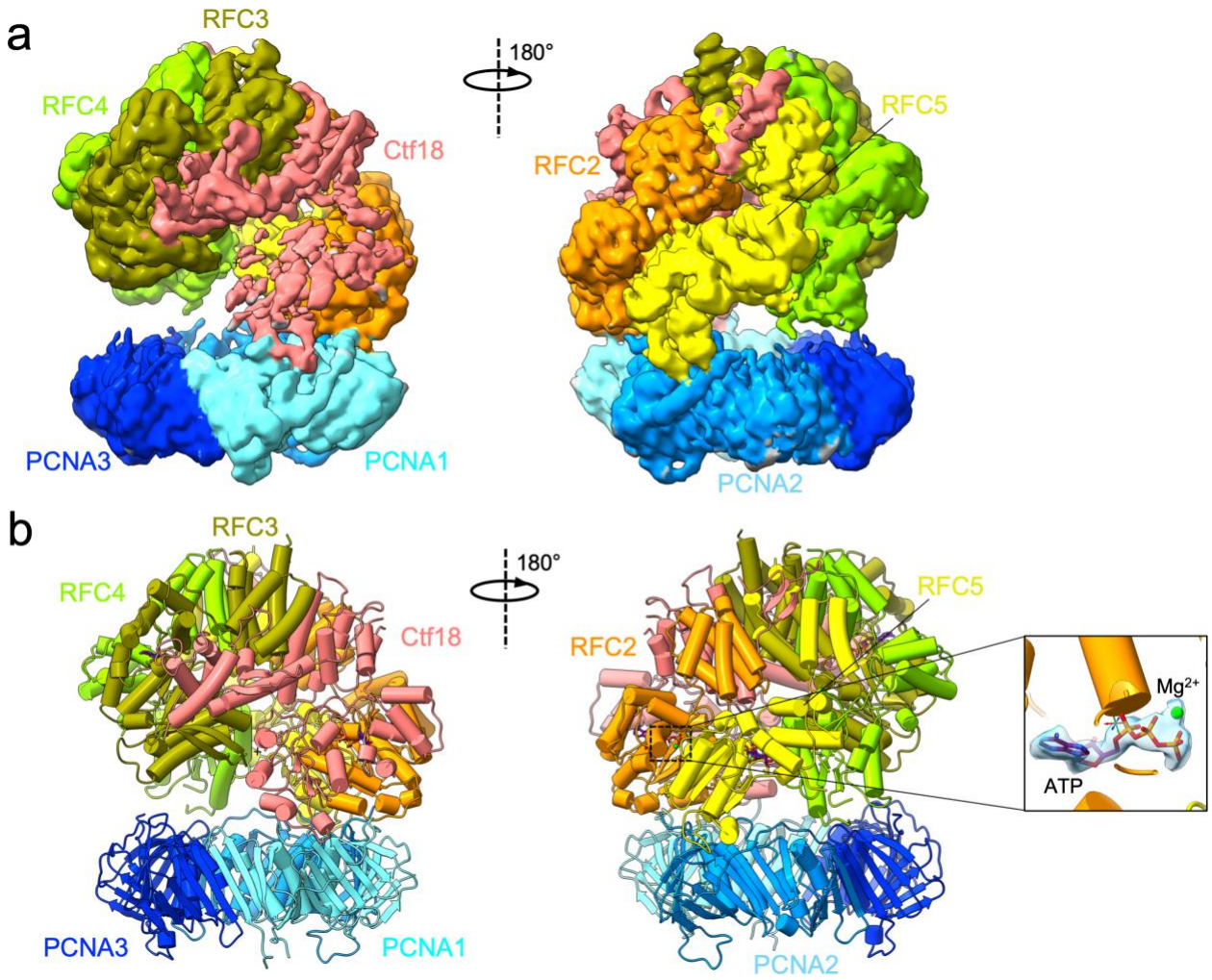

747

748

749 **Figure 5**. ***Cryo-EM structure of the human CTF18-RFC–PCNA complex in the***

750 ***presence of ATP and Mg^{2+}.*** **a)** Two views of the Cryo-EM map, coloured by subunits. **b)**

751 Molecular model in ribbon representation. The inset shows a map and model of the ATP

752 molecule bound to the RFC2 subunit, with a discernible Mg^{2+} ion.

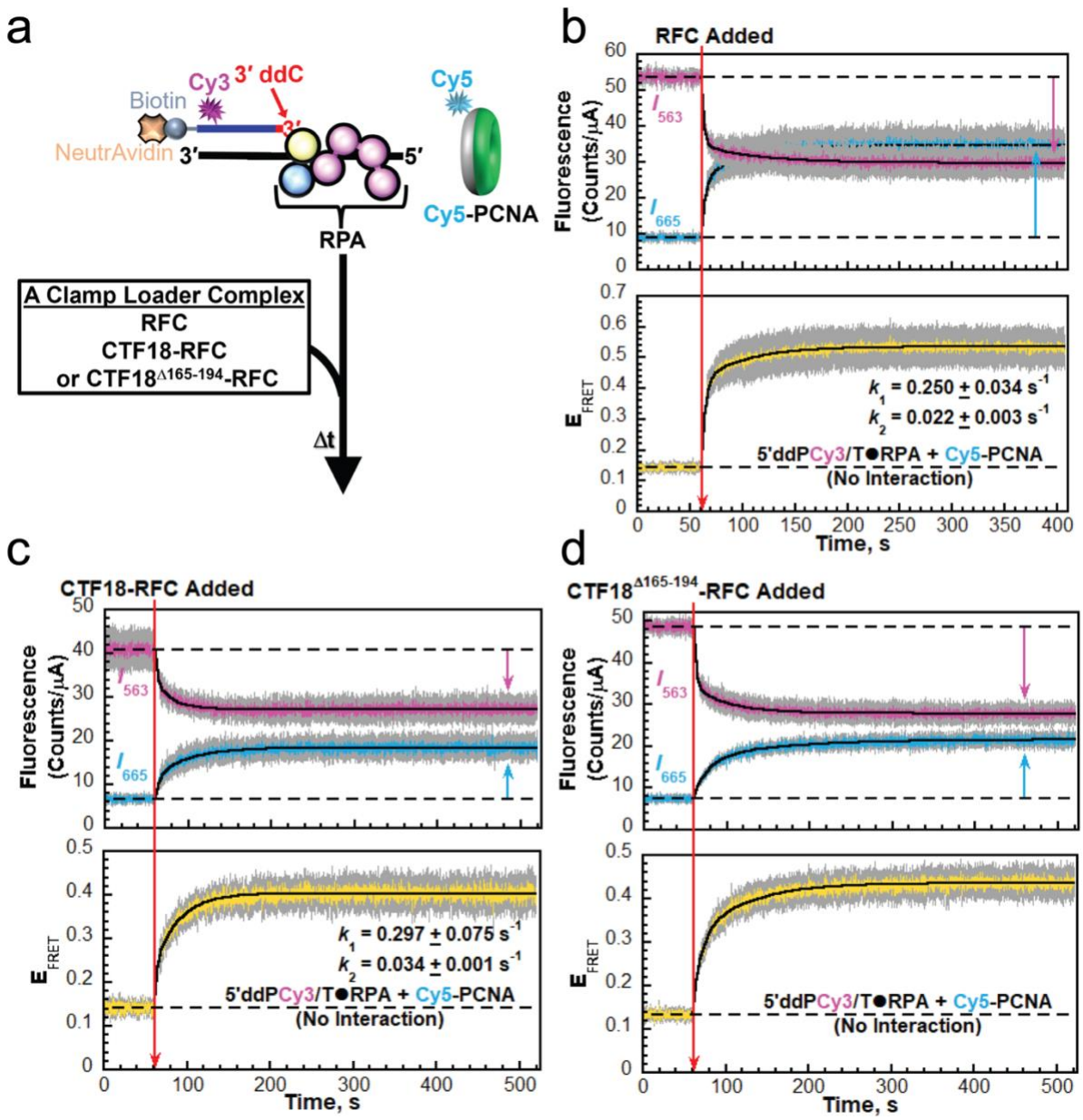

753

754 **Figure 6**. ***Loading of PCNA onto P/T junctions by human clamp loader complexes***.

755 **a)** Schematic representation of the FRET pair and experiment to monitor loading of Cy5-

756 PCNA onto 5′ddPCy3/T DNA substrates engaged by RPA. The front and back faces of

757 PCNA are displayed in green and grey, respectively. When loaded onto a 5′ddPCy3/T

758 DNA substrate, the Cy5 label on the back face of PCNA is oriented towards the Cy3 label

759 near the blunt duplex end of the 5′ddPCy3/T DNA substrate, yielding a FRET signal. **b** -

760 **d**) Data. Each trace is the mean of at least three independent traces with the S.E.M.
761 shown in grey. The time trajectories of I_{563} (magenta) and I_{665} (cyan) are displayed in the
762 top panels and the corresponding E_{FRET} (mustard) is displayed in the bottom panels. The
763 time at which a clamp loader complex is added is indicated by a red arrow. Changes in
764 I_{563} and I_{665} are indicated in the top panel by magenta and cyan arrows, respectively. The
765 I_{563}, I_{665}, and the corresponding E_{FRET} values observed prior to the addition of clamp
766 loader complexes represents the complete absence of interactions between
767 5¢ddPCy3/T·RPA complexes and Cy5-PCNA. For observations, these values are each
768 fit to flat line that is extrapolated to the axis limits. For observation, the I_{563} and I_{665} values
769 observed after the addition of clamp loader complexes are fit to double exponential
770 declines (I_{563}) and rises (I_{665}), respectively. The E_{FRET} values observed after the addition
771 of a given clamp loader are fit to double exponential rises and the respective rate
772 constants (k_1 and k_2) are reported in the corresponding figure and in **Table 1**. Data for
773 loading of PCNA by RFC, CTF18-RFC, and CTF18 $^{\Delta 165\text{-}194}$ -RFC are displayed in panels
774 **b**, **c**, and **d**, respectively.
775

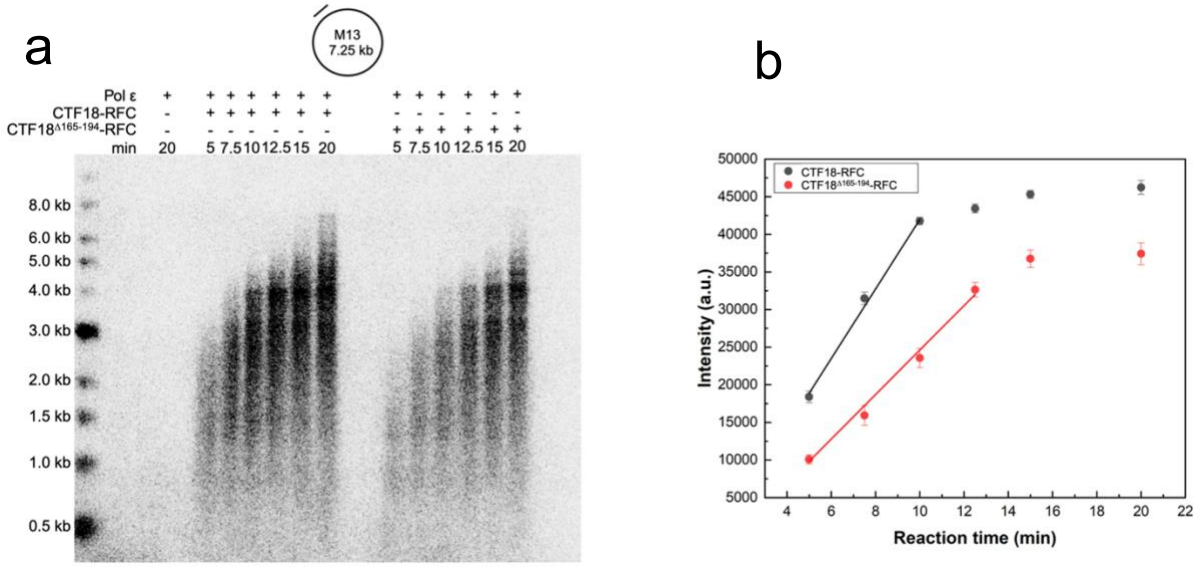

Figure 7. ***Primer extension assay with Pol ε and CTF18-RFC WT or CTF18$^{\Delta 165\text{-}194}$-RFC.*** **a)** Time course reactions on M13mp18 single-strand DNA with 40 nM wildtype CTF18-RFC or CTF18 $^{\Delta 165\text{-}194}$-RFC. Reactions were performed as described in Materials and Methods. **b)** Quantification of the band intensities from the primer extension assay shows that the rate of increase in intensity, derived from the initial linear portion of the reaction time before saturation, is 4142 ± 95 a.u./min for CTF18-RFC and 2389 ± 143 a.u./min for CTF18 $^{\Delta 165\text{-}194}$-RFC. This indicates that the mutant slows Pol ε synthesis by 42%. The experiment was conducted three times. Dots in **b)** represent mean values from the three replicas.

a

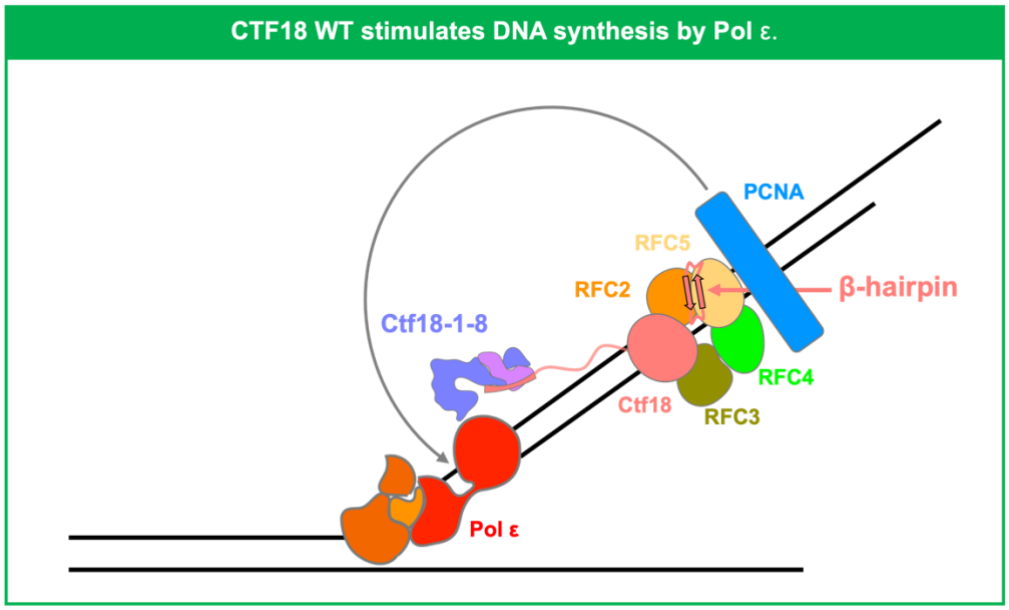

792

793

b

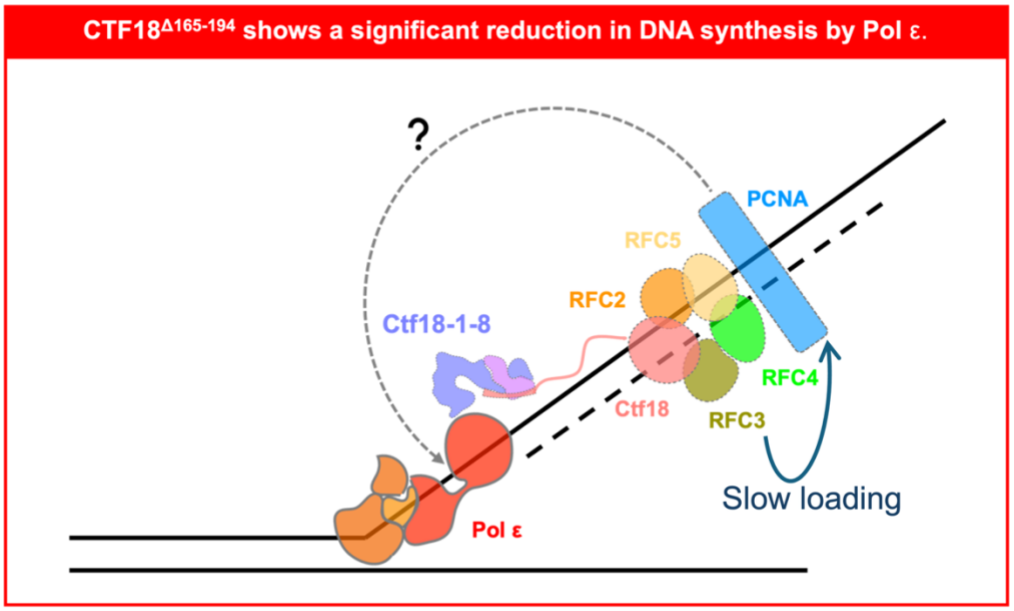

794

795 **Figure 8.** ***Deletion of the N-terminal β-hairpin in the Ctf18 large subunit slows down***

796 ***PCNA loading and reduces DNA synthesis by Pol ε.*** **a)** The structure of the RFC

797 module of CTF18-RFC is stabilized by the presence of a β-hairpin in the Ctf18 subunit

798 (amino acids 165-194). Thus, wild type CTF18-RFC loads PCNA onto DNA efficiently and

799 stimulates DNA synthesis by Pol ε interacting with the polymerase. **b)** The stability of the
800 CTF18-RFC–PCNA complex is diminished by the deletion of the β-hairpin. Consequently,
801 a CTF18-RFC deletion mutant lacking the β-hairpin (CTF18$^{\Delta 165\text{-}194}$-RFC) shows slower
802 loading of PCNA and lower activity in stimulating primer synthesis by Pol ε.
803
804
805
806
807
808
809
810
811
812
813
814
815
816
817
818
819
820
821

Clamp Loader	Kinetic Variables			
	A_1/A_T	k_1, s^{-1}	A_2/A_T	k_2, s^{-1}
RFC	0.728 ± 0.033	0.250 ± 0.034	0.272 ± 0.033	0.022 ± 0.003
CTF18-RFC	0.356 ± 0.028	0.297 ± 0.075 (1.00)	0.644 ± 0.028	0.034 ± 0.001 (1.00)
CTF18$^{\Delta 165\text{-}194}$-RFC	0.557 ± 0.023	0.108 ± 0.007 (0.36)	0.443 ± 0.023	0.017 ± 0.001 (0.49)

Table 1. Kinetic variables for loading of PCNA by human clamp loader complexes. Kinetic variables are from the fits to double exponential rises for the data presented in Figure 6 in the main text. The values in parentheses indicate the relationship (as a fraction) between the rate constants observed for CTF18-RFC and CTF18$^{\Delta 165\text{-}194}$-RFC.

References

1. Hubscher U, Maga G, Spadari S. Eukaryotic DNA polymerases. Annu Rev Biochem. 2002;71:133-63.
2. Choe KN, Moldovan GL. Forging Ahead through Darkness: PCNA, Still the Principal Conductor at the Replication Fork. Mol Cell. 2017;65(3):380-92.
3. Moldovan GL, Pfander B, Jentsch S. PCNA controls establishment of sister chromatid cohesion during S phase. Mol Cell. 2006;23(5):723-32.
4. Indiani C, O'Donnell M. The replication clamp-loading machine at work in the three domains of life. Nat Rev Mol Cell Biol. 2006;7(10):751-61.
5. Kelch BA, Makino DL, O'Donnell M, Kuriyan J. Clamp loader ATPases and the evolution of DNA replication machinery. Bmc Biology. 2012;10.
6. Kang MS, Ryu E, Lee SW, Park J, Ha NY, Ra JS, et al. Regulation of PCNA cycling on replicating DNA by RFC and RFC-like complexes. Nature Communications. 2019;10.
7. Jeruzalmi D, O'Donnell M, Kuriyan J. Crystal structure of the processivity clamp loader gamma (γ) complex of
DNA polymerase III. Cell. 2001;106(4):429-41.
8. Bowman GD, O'Donnell M, Kuriyan J. Structural analysis of a eukaryotic sliding DNA clamp-clamp loader complex. Nature. 2004;429(6993):724-30.
9. Kazmirski SL, Podobnik M, Weitze TF, O'Donnelll M, Kuriyan J. Structural analysis of the inactive state of the
DNA polymerase clamp-loader complex. Proceedings of the National Academy of Sciences of the United States of America. 2004;101(48):16750-5.
10. Gaubitz C, Liu XC, Magrino J, Stone NP, Landeck J, Hedglin M, et al. Structure of the human clamp loader reveals an autoinhibited conformation of a substrate-bound AAA plus switch. Proceedings of the National Academy of Sciences of the United States of America. 2020;117(38):23571-80.
11. Gaubitz C, Liu XC, Pajak J, Stone NP, Hayes JA, Demo G, et al. Cryo-EM structures reveal high-resolution mechanism of a DNA polymerase sliding clamp loader. Elife. 2022;11.
12. Schrecker M, Castaneda JC, Devbhandari S, Kumar C, Remus D, Hite RK. Multistep loading of a DNA sliding clamp onto DNA by replication factor C. Elife. 2022;11.
13. Turner J, Hingorani MM, Kelman Z, O'Donnell M. The internal workings of a DNA polymerase clamp-loading machine. EMBO J. 1999;18(3):771-83.
14. Gomes XV, Schmidt SL, Burgers PM. ATP utilization by yeast replication factor C. II. Multiple stepwise ATP binding events are required to load proliferating cell nuclear antigen onto primed DNA. J Biol Chem. 2001;276(37):34776-83.
15. Chen S, Levin MK, Sakato M, Zhou Y, Hingorani MM. Mechanism of ATP-driven PCNA clamp loading by S. cerevisiae RFC. J Mol Biol. 2009;388(3):431-42.
16. Simonetta KR, Kazmirski SL, Goedken ER, Cantor AJ, Kelch BA, McNally R, et al. The mechanism of ATP-dependent primer-template recognition by a clamp loader complex. Cell. 2009;137(4):659-71.
17. Kelch BA, Makino DL, O'Donnell M, Kuriyan J. How a DNA polymerase clamp loader opens a sliding clamp. Science. 2011;334(6063):1675-80.

879 18. Kelch BA. Review: The lord of the rings: Structure and mechanism of the sliding clamp
880 loader. Biopolymers. 2016;105(8):532-46.
881 19. Jeruzalmi D, O'Donnell M, Kuriyan J. Clamp loaders and sliding clamps. Curr Opin Struct
882 Biol. 2002;12(2):217-24.
883 20. Lee KY, Park SH. Eukaryotic clamp loaders and unloaders in the maintenance of genome
884 stability. Exp Mol Med. 2020;52(12):1948-58.
885 21. Mayer ML, Gygi SP, Aebersold R, Hieter P. Identification of RFC(Ctf18p, Ctf8p, Dcc1p): an
886 alternative RFC complex required for sister chromatid cohesion in S. cerevisiae. Mol Cell.
887 2001;7(5):959-70.
888 22. Naiki T, Kondo T, Nakada D, Matsumoto K, Sugimoto K. Chl12 (Ctf18) forms a novel
889 replication factor C-related complex and functions redundantly with Rad24 in the DNA replication
890 checkpoint pathway. Mol Cell Biol. 2001;21(17):5838-45.
891 23. Bylund GO, Burgers PM. Replication protein A-directed unloading of PCNA by the Ctf18
892 cohesion establishment complex. Mol Cell Biol. 2005;25(13):5445-55.
893 24. Crabbe L, Thomas A, Pantesco V, De Vos J, Pasero P, Lengronne A. Analysis of replication
894 profiles reveals key role of RFC-Ctf18 in yeast replication stress response. Nat Struct Mol Biol.
895 2010;17(11):1391-7.
896 25. Liu HW, Bouchoux C, Panarotto M, Kakui Y, Patel H, Uhlmann F. Division of Labor between
897 PCNA Loaders in DNA Replication and Sister Chromatid Cohesion Establishment. Mol Cell.
898 2020;78(4):725-38 e4.
899 26. al-Khodairy F, Carr AM. DNA repair mutants defining G2 checkpoint pathways in
900 Schizosaccharomyces pombe. EMBO J. 1992;11(4):1343-50.
901 27. Kim J, Robertson K, Mylonas KJ, Gray FC, Charapitsa I, MacNeill SA. Contrasting effects of
902 Elg1-RFC and Ctf18-RFC inactivation in the absence of fully functional RFC in fission yeast. Nucleic
903 Acids Res. 2005;33(13):4078-89.
904 28. Bermudez VP, Lindsey-Boltz LA, Cesare AJ, Maniwa Y, Griffith JD, Hurwitz J, et al. Loading
905 of the human 9-1-1 checkpoint complex onto DNA by the checkpoint clamp loader hRad17-
906 replication factor C complex in vitro. Proc Natl Acad Sci U S A. 2003;100(4):1633-8.
907 29. Terret ME, Sherwood R, Rahman S, Qin J, Jallepalli PV. Cohesin acetylation speeds the
908 replication fork. Nature. 2009;462(7270):231-4.
909 30. Zhang J, Shi X, Li Y, Kim BJ, Jia J, Huang Z, et al. Acetylation of Smc3 by Eco1 is required for
910 S phase sister chromatid cohesion in both human and yeast. Mol Cell. 2008;31(1):143-51.
911 31. Rolef Ben-Shahar T, Heeger S, Lehane C, East P, Flynn H, Skehel M, et al. Eco1-dependent
912 cohesin acetylation during establishment of sister chromatid cohesion. Science.
913 2008;321(5888):563-6.
914 32. Unal E, Heidinger-Pauli JM, Kim W, Guacci V, Onn I, Gygi SP, et al. A molecular determinant
915 for the establishment of sister chromatid cohesion. Science. 2008;321(5888):566-9.
916 33. Kubota T, Nishimura K, Kanemaki MT, Donaldson AD. The Elg1 replication factor C-like
917 complex functions in PCNA unloading during DNA replication. Mol Cell. 2013;50(2):273-80.
918 34. Stokes K, Winczura A, Song B, Piccoli G, Grabarczyk DB. Ctf18-RFC and DNA Pol ϵ form a
919 stable leading strand polymerase/clamp loader complex required for normal and perturbed DNA
920 replication. Nucleic Acids Res. 2020;48(14):8128-45.

921 35. Bermudez VP, Maniwa Y, Tappin I, Ozato K, Yokomori K, Hurwitz J. The alternative Ctf18-
922 Dcc1-Ctf8-replication factor C complex required for sister chromatid cohesion loads proliferating
923 cell nuclear antigen onto DNA. Proc Natl Acad Sci U S A. 2003;100(18):10237-42.
924 36. Fujisawa R, Ohashi E, Hirota K, Tsurimoto T. Human CTF18-RFC clamp-loader complexed
925 with non-synthesising DNA polymerase epsilon efficiently loads the PCNA sliding clamp. Nucleic
926 Acids Res. 2017;45(8):4550-63.
927 37. Grabarczyk DB, Silkenat S, Kisker C. Structural Basis for the Recruitment of Ctf18-RFC to
928 the Replisome. Structure. 2018;26(1):137-44 e3.
929 38. Jones ML, Baris Y, Taylor MRG, Yeeles JTP. Structure of a human replisome shows the
930 organisation and interactions of a DNA replication machine. EMBO J. 2021;40(23):e108819.
931 39. Langston LD, Zhang D, Yurieva O, Georgescu RE, Finkelstein J, Yao NY, et al. CMG helicase
932 and DNA polymerase epsilon form a functional 15-subunit holoenzyme for eukaryotic leading-
933 strand DNA replication. Proc Natl Acad Sci U S A. 2014;111(43):15390-5.
934 40. Yeeles JTP, Janska A, Early A, Diffley JFX. How the Eukaryotic Replisome Achieves Rapid
935 and Efficient DNA Replication. Mol Cell. 2017;65(1):105-16.
936 41. Chilkova O, Stenlund P, Isoz I, Stith CM, Grabowski P, Lundstrom EB, et al. The eukaryotic
937 leading and lagging strand DNA polymerases are loaded onto primer-ends via separate
938 mechanisms but have comparable processivity in the presence of PCNA. Nucleic Acids Res.
939 2007;35(19):6588-97.
940 42. Shahid T, Danazumi AU, Tehseen M, Alhudhali L, Clark AR, Savva CG, et al. Structural
941 dynamics of DNA unwinding by a replicative helicase. Nature. 2025;641(8061):240-9.
942 43. Punjani A, Rubinstein JL, Fleet DJ, Brubaker MA. cryoSPARC: algorithms for rapid
943 unsupervised cryo-EM structure determination. Nat Methods. 2017;14(3):290-6.
944 44. Punjani A, Fleet DJ. 3D variability analysis: Resolving continuous flexibility and discrete
945 heterogeneity from single particle cryo-EM. J Struct Biol. 2021;213(2):107702.
946 45. Jumper J, Evans R, Pritzel A, Green T, Figurnov M, Ronneberger O, et al. Highly accurate
947 protein structure prediction with AlphaFold. Nature. 2021;596(7873):583-9.
948 46. Cai J, Uhlmann F, Gibbs E, Flores-Rozas H, Lee CG, Phillips B, et al. Reconstitution of human
949 replication factor C from its five subunits in baculovirus-infected insect cells. Proc Natl Acad Sci U
950 S A. 1996;93(23):12896-901.
951 47. Podust VN, Tiwari N, Ott R, Fanning E. Functional interactions among the subunits of
952 replication factor C potentiate and modulate its ATPase activity. J Biol Chem. 1998;273(21):12935-
953 48. Cai J, Yao N, Gibbs E, Finkelstein J, Phillips B, O'Donnell M, et al. ATP hydrolysis catalyzed
954 by human replication factor C requires participation of multiple subunits. Proc Natl Acad Sci U S
955 A. 1998;95(20):11607-12.
956 49. Schmidt SL, Gomes XV, Burgers PM. ATP utilization by yeast replication factor C. III. The
957 ATP-binding domains of Rfc2, Rfc3, and Rfc4 are essential for DNA recognition and clamp loading.
958 J Biol Chem. 2001;276(37):34784-91.
959 50. Seybert A, Wigley DB. Distinct roles for ATP binding and hydrolysis at individual subunits
960 of an archaeal clamp loader. EMBO J. 2004;23(6):1360-71.
961 51. Sakato M, O'Donnell M, Hingorani MM. A central swivel point in the RFC clamp loader
962 controls PCNA opening and loading on DNA. J Mol Biol. 2012;416(2):163-75.

963 52. Liu J, Zhou Y, Hingorani MM. Linchpin DNA-binding residues serve as go/no-go controls in
964 the replication factor C-catalyzed clamp-loading mechanism. J Biol Chem. 2017;292(38):15892-
965 906.
966 53. He Q, Wang F, O'Donnell ME, Li H. Cryo-EM reveals a nearly complete PCNA loading
967 process and unique features of the human alternative clamp loader CTF18-RFC. Proc Natl Acad
968 Sci U S A. 2024;121(18):e2319727121.
969 54. Yuan Z, Georgescu R, Yao NY, Yurieva O, O'Donnell ME, Li H. Mechanism of PCNA loading
970 by Ctf18-RFC for leading-strand DNA synthesis. Science. 2024;385.
971 55. Henricksen LA, Umbricht CB, Wold MS. Recombinant replication protein A: expression,
972 complex formation, and functional characterization. J Biol Chem. 1994;269(15):11121-32.
973 56. Hedglin M, Perumal SK, Hu Z, Benkovic S. Stepwise assembly of the human replicative
974 polymerase holoenzyme. Elife. 2013;2:e00278.
975 57. Li M, Sengupta B, Benkovic SJ, Lee TH, Hedglin M. PCNA Monoubiquitination Is Regulated
976 by Diffusion of Rad6/Rad18 Complexes along RPA Filaments. Biochemistry. 2020;59(49):4694-
977 702.
978 58. Norris JL, Rogers LO, Pytko KG, Dannenberg RL, Perreault S, Kaushik V, et al. Replication
979 protein A dynamically re-organizes on primer/template junctions to permit DNA polymerase delta
980 holoenzyme assembly and initiation of DNA synthesis. Nucleic Acids Res. 2024.
981 59. Norris JL, Hedglin M. Direct, ensemble FRET approaches to monitor transient state kinetics
982 of human DNA polymerase delta holoenzyme assembly and initiation of DNA synthesis. Methods
983 Enzymol. 2024;705:271-309.
984 60. Zheng SQ, Palovcak E, Armache JP, Verba KA, Cheng Y, Agard DA. MotionCor2: anisotropic
985 correction of beam-induced motion for improved cryo-electron microscopy. Nat Methods.
986 2017;14(4):331-2.
987 61. Rohou A, Grigorieff N. CTFFIND4: Fast and accurate defocus estimation from electron
988 micrographs. J Struct Biol. 2015;192(2):216-21.
989 62. Kimanius D, Dong L, Sharov G, Nakane T, Scheres SHW. New tools for automated cryo-EM
990 single-particle analysis in RELION-4.0. Biochem J. 2021;478(24):4169-85.
991 63. Bepler T, Morin A, Rapp M, Brasch J, Shapiro L, Noble AJ, et al. Positive-unlabeled
992 convolutional neural networks for particle picking in cryo-electron micrographs. Nat Methods.
993 2019;16(11):1153-60.
994 64. Kelley LA, Mezulis S, Yates CM, Wass MN, Sternberg MJ. The Phyre2 web portal for protein
995 modeling, prediction and analysis. Nat Protoc. 2015;10(6):845-58.
996 65. Emsley P, Lohkamp B, Scott WG, Cowtan K. Features and development of Coot. Acta
997 Crystallogr D Biol Crystallogr. 2010;66(Pt 4):486-501.
998 66. Croll TI. ISOLDE: a physically realistic environment for model building into low-resolution
999 electron-density maps. Acta Crystallogr D Struct Biol. 2018;74(Pt 6):519-30.
1000 67. Adams PD, Afonine PV, Bunkoczi G, Chen VB, Davis IW, Echols N, et al. PHENIX: a
1001 comprehensive Python-based system for macromolecular structure solution. Acta Crystallogr D
1002 Biol Crystallogr. 2010;66(Pt 2):213-21.

1003